DYNAMIC MOTION CONTROL FOR COMPLIANT FRAMED WHEELED MODULAR MOBILE ROBOTS

by

Xiaorui Zhu

A dissertation submitted to the faculty of
The University of Utah
in partial fulfillment of the requirements for the degree of

Doctor of Philosophy

Department of Mechanical Engineering

The University of Utah

December 2006

THE UNIVERSITY OF UTAH GRADUATE SCHOOL

SUPERVISORY COMMITTEE APPROVAL

of a dissertation submitted by

Xiaorui Zhu

This dissertation has been read by each member of the following supervisory committee and by majority vote has been found to be satisfactory.

_____	_____
	Chair: Mark A. Minor
_____	_____
	Marc Bodson
_____	_____
	Mikhail Skliar
_____	_____
	Sanford G. Meek
_____	_____
	Stacy Morris Bamberg

THE UNIVERSITY OF UTAH GRADUATE SCHOOL

FINAL READING APPROVAL

To the Graduate Council of the University of Utah:

I have read the dissertation of Xiaorui Zhu in its final form and have found that (1) its format, citations and bibliographic style are consistent and acceptable; (2) its illustrative materials including figures, tables and charts are in place; and (3) the final manuscript is satisfactory to the supervisory committee and is ready for submission to The Graduate School.

_____ _____

Date Mark A. Minor
Chair, Supervisory Committee

Approved for the Major Department

_____

Kent S. Udell
Department Chair

Approved for the Graduate Council

_____

David S. Chapman
Dean of The Graduate School

ABSTRACT

In this dissertation, a distributed robust controller, a motion control and sensing architecture, and a terrain feature localization are studied to solve general navigation problems for Compliant Framed wheeled Modular Mobile Robots (CFMMR). This type of wheeled mobile robot uses rigid axles coupled by compliant frame modules to provide both full suspension and enhanced steering capability without additional hardware.

First, a distributed nonlinear damping controller is developed for single-axle unicycle type robots. The controller is then extended to multiple-axle CFMMR configurations and is robust to disturbances created by modeling errors, especially highly nonlinear frame forces caused by axle interaction. In particular, the controller considers time-varying reference velocities and allows the robot to perform posture regulation, path following, or general trajectory tracking.

In order to achieve improved motion control of CFMMR, a distributed cooperative motion control and sensing architecture is developed by combining a kinematic controller for motion coordination and providing reference commands, dynamic motion controllers to follow these commands and reject disturbances, and a sensor fusion system to provide accurate posture estimates. Requirements for each subsystem and their respective interconnections are defined to optimize system performance.

Simulations and experiments on a two-axle CFMMR verify robust dynamic motion control of path following and improved motion control of posture regulation under the developed control and sensing architecture.

The largest source of error in the above work is due to localization. Thus, a novel terrain feature localization technique is proposed to allow the robot to identify its location relative to measurable terrain characteristics. A terrain inclination map is extracted from a given topographical map along a specific path. An EKF is used to fuse the measurement data with the robot motion based on the extracted terrain map. Simulations validate the proposed terrain localization technique.

In this dissertation, three major aspects of robot motion control are studied. The control architecture provides a frame work for implementing motion control. The robust controller is a key part of this architecture and improves accuracy while the localization algorithm improves precision. While the target platform is CFMMR, these strategies represent fundamental advancements in robot motion control.

To my dear husband, Jun Lin, and my lovely daughter, Melody Tongxi Lin.

TABLE OF CONTENTS

ACKNOWLEGEMENTS

I am honored to work with Professor Mark Minor. I appreciate him for his consistent help over the past several years, for teaching me about the research process, for providing helpful guidance on my career plan, and for giving very thoughtful suggestions on this project.

I have been lucky to work with many nice people in the Robotics System Laboratory and the Mechanical Engineering Department. Special thanks to Youngshik Kim for his help throughout this project.

Most importantly, I thank my husband Jun and my parents Jinliang and Qinghuan for their endless support. Without my husband's patience and support, I would not have even started my studies in the United States. Without my parents helping me to take care of my daughter, I would have not finished this project.

This work was supported by NSF Grant IIS-0308056.

CHAPTER 1

INTRODUCTION

Motion control of Compliant Framed Modular Mobile Robots (CFMMR), shown in Figure 1.1, is the subject of this research. The CFMMR has uniqueness in modularity, simple structure and adaptability because it uses compliant frame coupling to provide suspension and steering based on the rigid axle modules with independently controlled wheels. Despite these attributes, the compliant frames provide new challenges in accurate motion control and general navigation issues. First, the compliant frame coupling provides more physical constraints in the robot kinematics. Second, the nonlinear interaction forces created by the compliant frame are considerable in the dynamics of the robot. Third, the compliant coupling also requires the sensory system to provide more accurate estimates to reduce interaction forces. In order to address these

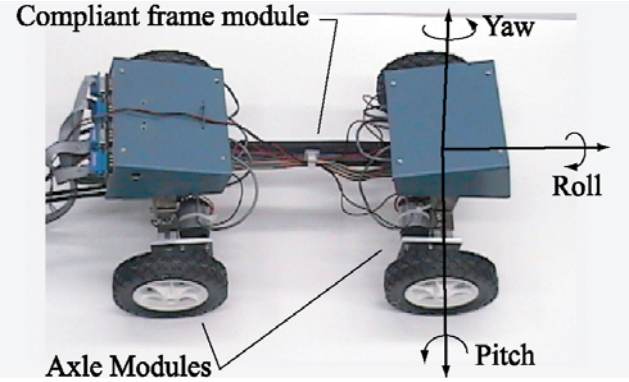

Figure 1.1. Two-axle CFMMR.

challenges, two journal papers are introduced in Chapter 2 and Chapter 3. The general motivations and contributions are discussed in the following paragraphs while the detailed background of the individual work will be provided in each chapter.

Chapter 2 is a journal paper published in the ASME Journal of Dynamic Systems, Measurement, and Control. In this paper, a distributed nonlinear damping robust dynamic controller is first proposed to deal with highly nonlinear compliant frame forces in the presence of unmodeled disturbances. Using backstepping techniques, the wheel-torque controller is developed for single-axle module and then extended to multiaxle configurations. The compliant frame forces are estimated based on the Finite Element Method and the postbuckled frame element. These estimates are included in the control design to reduce tracking error and aggressiveness of the controller. Time-varying reference trajectories are also considered in the control design such that the dynamic controller can be combined with a kinematic motion controller for overall cooperative control of the CFMMR. Simulation and experiments were conducted on carpet for a two-axle CFMMR to perform path following. The corresponding results verify robustness of the proposed dynamic controller.

The major contribution of this chapter is development of model-based distributed robust control for the CFMMR, which is generally applicable to any cooperative mobile robotic system with uncertain compliant interaction forces. Two significant issues considered in the development of the controller are modeling and control of highly nonlinear interaction forces, and dynamic tracking control of time-varying reference trajectories (velocity and posture specified as a function of time by a *kinematic motion controller*). As part of the major contribution, the distributed robust controller

performance is experimentally validated with and without interaction force models and its capability to track time varying trajectories is illustrate.

In order to improve robot motion control based upon the robust dynamic motion controller, another focus of this research is a cooperative motion control and sensing architecture, Figure 1.2, of the two-axle CFMMR. The architecture consists of kinematic motion control, dynamic motion control and sensor fusion system components for solving all the kinematics, dynamics and sensing problems of overall robotic motion control. The detailed work will be discussed in Chapter 3. This chapter is a journal paper conditionally accepted by the IEEE Transactions on Robotics. In this paper, based on ideal kinematics, a centralized kinematic motion controller is used to manage axle cooperation in lieu of physical constraints imposed by the wheels and the compliant frames, and provides bounded reference posture and velocities. The distributed dynamic controller then tracks these references such that physical constraints are satisfied during movement of the robot in lieu of disturbances. A distributed sensory system includes a relative position sensor

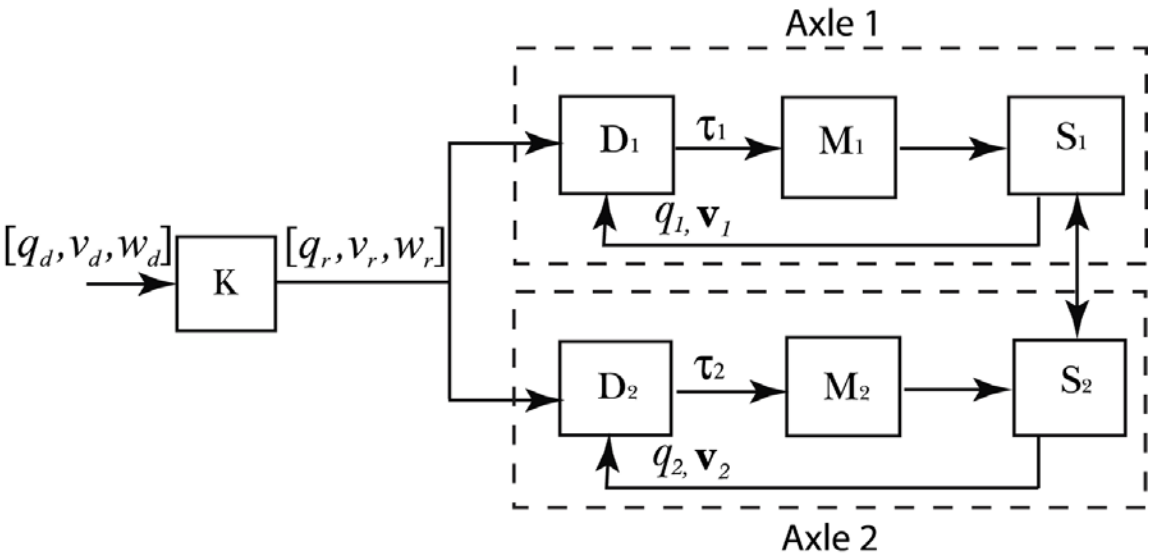

Figure 1.2. Motion control and sensing architecture.

within a tiered fusion algorithm to provide accurate posture and velocity estimates, which reduces interaction forces due to off-tracking between neighboring axles. Algorithms and controllers for each component that satisfy these requirements are then implemented and evaluated on a two-axle CFMMR. In particular, the distributed nonlinear damping robust dynamic controller mentioned above is used to implement the dynamic motion control component. The system performance was conducted on surfaces with increasing roughness, such as carpet, sand, and sand with scattered rocks for posture regulation. Several other suboptimal configurations were also evaluated to compare with the proposed architecture. Based upon 35 individual tests, the results validate superiority of the proposed architecture.

The main contributions of this chapter involve a distributed cooperative motion control and sensing architecture. The architecture and requirements for the kinematic controller, dynamic controller, and sensor system components are specified in order to reduce tracking error in lieu of robot interaction forces and unmodeled disturbances. Algorithms and controllers for each component that satisfy these requirements are then implemented and the architecture is evaluated experimentally. While the target application is the CFMMR, this architecture is easily extended to any cooperative mobile robotic system. Further, given the modular structure of the architecture, it is easy to customize specific components to satisfy navigation requirements of the robot and to allow a team to design the components in parallel for faster implementation.

Since localization is always challenging to mobile robots operating on rough terrain, the third part of the research provides a terrain feature based localization technique to allow the robots to localize themselves relative to measurable terrain

characteristics such as terrain inclination and surface roughness. It is assumed that a specified path is preselected on a topographical map according to the operator's judgment, and that obstacles and borders are identified in the map. An elevation map is then obtained along a vertical plane crossing the chosen path. Based on this elevation map, a terrain inclination map is extracted along that path. Unlike traditional techniques where physical landmarks define features in the map, terrain inclination is treated as the localization feature of the environment. A tilt sensor is used to measure the terrain inclination, and an Extended Kalman Filter (EKF) is used to incorporate the data to estimate the position of the robot given the extracted terrain map. Simulation results indicate that the proposed technique has the capability to reject bias and system noise to improve localization.

The main contribution of this part involves a terrain feature based localization technique to allow the robot to identify its position relative to a terrain characteristic map. A terrain map extraction algorithm is derived to extract terrain inclination information from a topographical map. An EKF algorithm is specially applied to achieve terrain feature localization based on the extracted terrain map. Thus, this research contributes a new method of localizing robot position. This terrain feature localization technique is generally applicable to other two-axle mobile robots even though the intended platform is the CFMMR.

In this dissertation, the three topics of robust motion control, control and sensing architecture and terrain localization are investigated. The motion control and sensing architecture provides a frame work to integrate the kinematic controller, dynamic controller, and sensor fusion system to achieve better mobile robot performance. The

distributed robust dynamic controller rejects modeling disturbances with unknown bounds and improves the tracking accuracy as a key part of the motion control and sensing architecture. The terrain feature localization technique improves the position precision of the mobile robot on uneven terrain. Although the algorithms are applied to CFMMR, they can be easily extended to other mobile robotic systems. As a result, the three aspects of this dissertation represent fundamental advancements in robot motion control.

The structure of the proposal follows. In Chapter 2, a distributed robust dynamic motion controller is derived, and performance evaluation is presented and discussed. In Chapter 3, a cooperative motion control and sensing architecture is proposed and evaluated. A terrain feature localization technique is proposed and simulated in Chapter 4. Conclusions are made in Chapter 5.

CHAPTER 2

DISTRIBUTED ROBUST DYNAMIC MOTION CONTROLLER

This chapter is a journal paper published in the ASME Journal of Dynamic Systems, Measurement, and Control, Vol. 128, pp. 489-498. Authors are Xiaorui Zhu, Sungyong Park, and Mark A. Minor.

Distributed Robust Control of Compliant Framed Wheeled Modular Mobile Robots

Xiaorui Zhu
ASME Student Member

Mark A. Minor
ASME Member
e-mail: minor@mech.utah.edu

Sungyong Park

Department of Mechanical Engineering,
University of Utah,
Salt Lake City, Utah 84112

A distributed robust controller for Compliant Framed wheeled Modular Mobile Robots (CFMMR) is studied in this paper. This type of wheeled mobile robot uses rigid axles coupled by compliant frame modules to provide both full suspension and enhanced steering capability without additional hardware. In this research, a distributed nonlinear damping controller using backstepping techniques for wheel-torque control is first developed for single-axle unicycle type robots. The controller is then extended to multiple-axle CFMMR configurations and is robust to disturbances created by modeling errors; especially highly nonlinear frame forces caused by axle interaction. In particular, the controller considers time-varying reference velocities and allows the robot to perform posture regulation, path following, or general trajectory tracking. A two-axle scout CFMMR configuration is used to evaluate the controller. Simulation and experimental results verify robust dynamic motion control of path following. [DOI: 10.1115/1.2229254]

1 Introduction

A distributed robust dynamic control algorithm for multi-axle Compliant Framed wheeled Modular Mobile Robots (CFMMR) is developed in this paper. A two-axle CFMMR, Fig. 1, is used for testing in the experiments. The CFMMR concept is unique in two ways. First, it uses a novel yet simple structure to provide suspension and highly controllable steering capability without any additional hardware. This is accomplished by compliant frame elements that couple rigid differentially steered axles. In this study, a partially compliant frame provides roll and yaw Degrees of Freedom (DOF) for suspension and steering capability, respectively. The CFMMR also improves the modularity of wheeled mobile robotics by allowing frame and axle modules to be assembled in configurations customized for specific tasks. It is argued that homogeneity reduces maintenance, offers increased robustness through redundancy, provides compact and ordered storage, and increases adaptability [1,2]. Despite these attributes, the CFMMR provides new challenges in motion control [3–5], sensor instrumentation [6], and data fusion [6].

A limited number of compliant vehicles have been investigated in the last few decades, and none possess a similar highly compliant frame whose deflection is controlled by coordinated actuation of the wheels. The earliest platform is a system proposed for planetary exploration using compliant members to provide roll and pitch DOF for suspension of the axles [7] to adapt to the terrain. More recent research has introduced compliance to accommodate measurement error and prevent wheel slip from occurring between independently controlled axle units on a service robot [8]. This robot is similar in spirit to the CFMMR in that it allows relative rotation between the axles, but this compliance is provided by rotary joints connected to the ends of a frame with limited prismatic compliance. Some snake-like robots also use wheeled body modules, but they are usually connected in series by articulated joints. Some have active joints and passive wheels [9] while others have active wheels and either partially active [10,11] or entirely passive joints [12]. Active wheels provide direct control over forward velocity and are better for traveling over terrain. Active joints allow direct control over robot shape, but they are too slow for high-speed movement. Active-wheel passive-joint snake-like robots, which are most similar to the CFMMR, are thus desirable for natural terrain adaptation and faster travel over rugged terrain [12]. Compared to the complex and expensive mechanical joints in all of these robots, the CFMMR is much simpler, and is thus less expensive and has less potential for mechanical failure.

The control of compliance in robotic systems has been predominant among flexible manipulators, where oscillations are a primary concern [13,14]. Compliance control in the CFMMR differs in two very substantial ways. First, the modeling structure presented here is unique because the compliant frames encounter large deflections and may operate within post-buckled configurations during steering maneuvers. Therefore, it is difficult to model the compliant frame forces with great accuracy, although an approximate model of the compliant frame is developed based on the Finite Element Method (FEM) and the post-buckled frame element [5]. Second, flexible manipulators do not posses nonholonomic constraints, which are one of the typical characteristics of the CFMMR. Hence, the dynamic controllers developed for the CFMMR must consider nonlinear compliance effects and nonholonomic constraints typical of mobile robots, which prevent the application of traditional dynamic controllers for flexible manipulators. Compliance among mobile robots cooperatively manipulating an object has also received attention [15,16], but these efforts have focused on motion planning and coordination issues rather than robust dynamic motion control subject to nonholonomic constraints, which is the subject of this paper. The controller derived here could certainly benefit cooperative mobile robots, though.

In recent years, much attention has been paid to the motion control of mobile robots. Some research focuses only on the kinematic model (e.g. steering system) of a mobile robot where the input is velocity [3,17], and these can be called *kinematic motion controllers*. However, practically they need to take into account the specific dynamics that can produce the input velocity using wheel torque provided by the mobile robot. Thus, some research has been oriented toward torque-based control of dynamical models combined with kinematic models subject to nonholomomic constraints in order to improve tracking performance [18,19], which can be regarded as *dynamic motion control*. These efforts have focused only on rigid mobile robots not interacting cooperatively with other robots.

Control of the CFMMR requires that we consider compliant coupling (e.g., cooperation) between multiple axle modules. Thus,

Contributed by the Dynamic Systems, Measurement, and Control Division of ASME for publication in the JOURNAL OF DYNAMIC SYSTEMS, MEASUREMENT, AND CONTROL. Manuscript received December 14, 2004; final manuscript received January 13, 2006. Assoc. Editor: Sunil K. Agrawal.

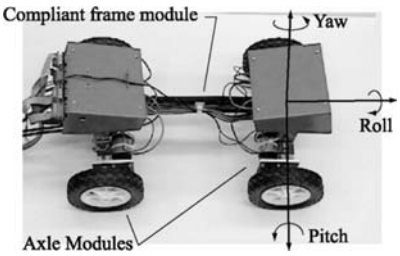

Fig. 1 Two-axle CFMMR experimental configuration

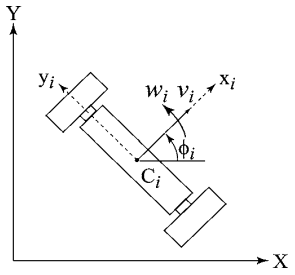

Fig. 2 The *i*th axle module kinematics

we use a curvature-based *kinematic motion controller* [3,4] to specify individual axle motion such that the CFMMR executes the desired net motion. These individual axle motions then provide real-time reference inputs to a *dynamic motion controller*. In our previous work, a perfect model of the CFMMR was assumed in the dynamic controller, which ultimately led to tracking error and necessary controller tuning for specific types of paths [5].

In reality, many kinds of disturbances always exist. Therefore, a few nonlinear, robust, and adaptive *dynamic motion control* techniques have been developed in the presence of the uncertainties of mobile robots [20–25] to confront the negative effects caused by approximation. Other researchers proposed discontinuous robust and/or adaptive controllers that complicate the adjustment of control gains to deal with instability caused by discontinuity, where the bounds of the uncertainties must be known [21–23]. Fierro proposed robust adaptive controllers using online neural networks. But a time-consuming computation is required, and it is difficult to guarantee the convergence of neural network controllers in real time [24,25]. Lin developed a robust damping control technique that does not require any knowledge of the bounds of the disturbances and had a fairly simple structure. Because of the complexity of the CFMMR dynamic model and the potentially large frame forces, the disturbances are unpredictable [20]. Hence, our robust controller is based on extension of [20]. Note that the reference velocities provided by our curvature-based *kinematic motion control* algorithms for posture regulation [3] and path following [4,26] are time varying, however, while constant reference velocities are assumed for simplicity in [20].

The major contribution of this work is development of model-based distributed robust control for the CFMMR, which is generally applicable to any cooperative mobile robotic system with uncertain compliant interaction forces. Two significant issues considered in the development of the controller are modeling and control of highly nonlinear interaction forces, which is novel, and dynamic tracking control of time-varying reference trajectories (velocity and posture specified as a function of time by a *kinematic motion controller*), which is an extension of previous work. As part of the major contribution, we experimentally validate the distributed robust controller performance with and without interaction force models and illustrate its capability to track time varying trajectories.

The structure of the paper follows. Modular kinematic and dynamic models of the CFMMR are derived in Sec. 2. A nonlinear damping controller for unicycle type robots with time varying reference velocities is proposed in Sec. 3. A distributed controller for general multi-module CFMMR configurations is proposed in Sec. 4. The distributed control algorithm is then applied to a two-axle CFMMR in simulation and experiment to evaluate their performance in Sec. 5. Concluding remarks and future work are described in Sec. 6.

2 Kinematic and Dynamic Models

2.1 Generic Modeling Structure. Consider the *i*th axle of an *n*-axle CFMMR, Fig. 2. Let us define a fixed global reference frame $F(X,Y)$ and moving frames $f_i(x_i,y_i)$ attached to the points C_i at the midpoint of the *i*th axle, where $i=1\ldots n$. At any instant, the *i*th axle module is rotating about the IC (Instantaneous Center), Fig. 3, such that the ICR's projections onto the x_i axes define point C_i at the midpoint of each axle. A module configuration vector $q_i=[X_i\ Y_i\ \phi_i]$ is then attached to this point and oriented with the axle. In order to describe this configuration within the context of the entire system, we assemble each of these module configuration vectors into a system configuration vector $Q=[q_1,\ldots,q_n]^T$ where $Q\in R^{3n\times 1}$. It is then possible to assemble a system description of the form,

$$\mathbf{M}(Q)\ddot{Q}+\mathbf{V}(Q,\dot{Q})\dot{Q}+\mathbf{F}(\dot{Q})+\mathbf{G}(Q)+\tau_d+\mathbf{F}_K(Q)=\mathbf{E}(Q)\tau-\mathbf{A}^T(Q)\lambda, \quad (1)$$

where $\mathbf{M}(Q)\in R^{3n\times 3n}$ is a symmetric, positive definite inertia matrix assembled from the individual axle module inertia matrices. Assembling individual axle module dynamic characteristics into the system model, $\mathbf{V}(Q,\dot{Q})\in R^{3n\times 3n}$ is the centripetal and coriolis forces, $\mathbf{F}(\dot{Q})\in R^{3n\times 1}$ denotes the friction, $\mathbf{G}(Q)\in R^{3n\times 1}$ is the gravitational vector, τ_d denotes bounded unknown disturbances including unstructured unmodeled dynamics, $\mathbf{E}(Q)\in R^{3n\times 2n}$ is the input transformation matrix, $\tau\in R^{2n\times 1}$ is the input torques, and $\lambda\in R^{n\times 1}$ is the vector of constraint forces. $\mathbf{A}(Q)\in R^{n\times 3n}$ is the global matrix associated with the nonholonomic constraints. Compliant frame forces are described by globally defined stiffness equations that are assembled into $\mathbf{F}_K(Q)\in R^{3n\times 1}$.

2.2 Modular Dynamic Models. First, the dynamic model of single-axle module is presented [18]. The generic matrices are then assembled assuming a serial configuration. Considering the *i*th axle module, we let $\mathbf{V}_i(q_i,\dot{q}_i)=\mathbf{0}$ since centripetal and coriolis

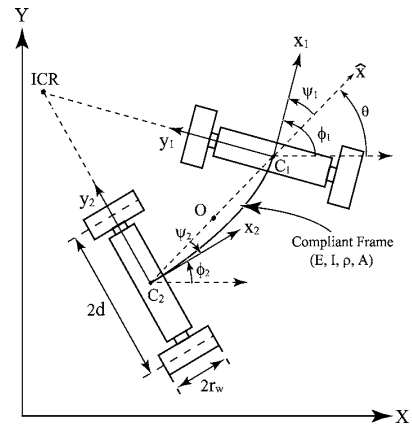

Fig. 3 General configuration of a two-axle CFMMR

forces of each axle are relatively small due to the velocity and curvature constraints of our robot. Also, $\mathbf{G}_i(q_i)=\mathbf{0}$ since motion of robot system is assumed to be in the horizontal plane. The mass matrix and the input transformation matrix of this axle module are:

$$\mathbf{M}_i(q_i)=\begin{bmatrix} m_i & 0 & 0 \\ 0 & m_i & 0 \\ 0 & 0 & J_i \end{bmatrix}, \quad \mathbf{E}_i(q_i)=\frac{1}{r_w}\begin{bmatrix} \cos\phi_i & \cos\phi_i \\ \sin\phi_i & \sin\phi_i \\ -d & d \end{bmatrix} \tag{2}$$

where m_i and J_i are mass and mass moment of the ith axle individually. The wheel torques applied to the ith axle module are denoted as $\tau_i=[\tau_{L,i}\ \tau_{R,i}]^T$, where $\tau_{L,i}$ and $\tau_{R,i}$ are motor torques acting on the left and right wheel, respectively. The corresponding frame reaction forces are then expressed as:

$$\mathbf{F}_{K,i}(q_i,q_j)=[F_{X,i}\ F_{Y,i}\ M_i]^T \tag{3}$$

where j denotes the numbers of all the axles connected with the ith axle, and the Lagrange multipliers are determined by,

$$\lambda_i=-m_i\dot{\phi}_i(\dot{X}_i\cos\phi_i+\dot{Y}_i\sin\phi_i)+F_{X,i}\sin\phi_i-F_{Y,i}\cos\phi_i \tag{4}$$

Therefore the ith axle dynamic equation is expressed as:

$$\mathbf{M}_i(q_i)\ddot{q}_i+\mathbf{F}(\dot{q}_i)+\tau_{d,i}+\mathbf{F}_{K,i}(q_i,q_j)=\mathbf{E}_i(q_i)\tau_i-\mathbf{A}_i^T(q_i)\lambda_i \tag{5}$$

Hence, the whole dynamic system is assembled by the above axle module matrices as:

$$\mathbf{M}(Q)=\begin{bmatrix} \mathbf{M}_1(q_1) & 0 & \cdots & 0 \\ 0 & \mathbf{M}_2(q_2) & 0 & \cdots \\ \cdots & 0 & \cdots & 0 \\ 0 & \cdots & 0 & \mathbf{M}_n(q_n) \end{bmatrix} \tag{6}$$

$$\mathbf{E}(Q)=\begin{bmatrix} \mathbf{E}_1(q_1) & 0 & \cdots & 0 \\ 0 & \mathbf{E}_2(q_2) & 0 & \cdots \\ \cdots & 0 & \cdots & 0 \\ 0 & \cdots & 0 & \mathbf{E}_n(q_n) \end{bmatrix} \tag{7}$$

$$\mathbf{F}_K(Q)=[\mathbf{F}_{K,1}\ \mathbf{F}_{K,2}\ \cdots\ \mathbf{F}_{K,n}]^T \tag{8}$$

$$\tau=[\tau_1\ \tau_2\ \cdots\ \tau_n]^T \tag{9}$$

2.3 Modular Kinematic Models. The kinematic model of the ith axle module is presented subject to nonholonomic constraints [18]. The generic kinematic matrices are then assembled similar to the dynamic matrices. Assuming pure rolling without slipping, the nonholonomic constraints of the ith axle module can be expressed in matrix form as

$$\mathbf{A}_i(q_i)\dot{q}_i=0 \tag{10}$$

where $\mathbf{A}_i(q_i)\in R^{1\times 3}$ is the matrix associated with the ith axle nonholonomic constraints:

$$\mathbf{A}_i(q_i)=[-\sin\phi_i\ \cos\phi_i\ 0] \tag{11}$$

Let $\mathbf{S}_i(q_i)\in R^{3\times 2}$ then be a full rank matrix formed by a set of smooth and linearly independent vector fields spanning the null space of $\mathbf{A}_i(q_i)$ such that

$$\mathbf{A}_i(q_i)\mathbf{S}_i(q_i)=\mathbf{0} \tag{12}$$

Equations (10) and (12) imply the existence of a two dimensional velocity vector $\mathbf{v}_i(t)\in R^{2\times 1}$ such that, for all time, t,

$$\dot{q}_i=\mathbf{S}_i(q_i)\mathbf{v}_i(t) \tag{13}$$

where

$$\mathbf{S}_i(q_i)=\begin{bmatrix} \cos\phi_i & 0 \\ \sin\phi_i & 0 \\ 0 & 1 \end{bmatrix} \tag{14}$$

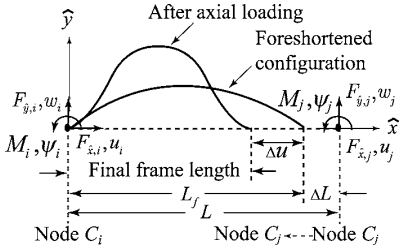

Fig. 4 The general configuration of single-finite-element of the compliant frame module

$$\mathbf{v}_i(t)=[v_i\ \omega_i]^T \tag{15}$$

and v_i and ω_i represent the linear and angular velocities of the ith axle at point C_i.

Likewise, the n-axle matrix associated with the nonholonomic for the serial configuration can be assembled as:

$$\mathbf{A}(Q)=\begin{bmatrix} \mathbf{A}_1(q_1) & \mathbf{0} & \cdots & \mathbf{0} \\ \mathbf{0} & \mathbf{A}_2(q_2) & \cdots & \vdots \\ \mathbf{0} & \mathbf{0} & \cdots & \mathbf{0} \\ \mathbf{0} & \cdots & \mathbf{0} & \mathbf{A}_n(q_n) \end{bmatrix} \tag{16}$$

There is also the existence of a $2n$ dimensional velocity vector $\mathbf{v}(t)\in R^{2n\times 1}$ such that, for all time, t,

$$\dot{Q}=\mathbf{S}(Q)\mathbf{v}(t) \tag{17}$$

where $\mathbf{S}(Q)\in R^{3n\times 2n}$ is a full rank matrix formed by a set of smooth and linearly independent vector fields spanning the null space of $\mathbf{A}(Q)$ such that

$$\mathbf{A}(Q)\mathbf{S}(Q)=\mathbf{0} \tag{18}$$

and $\mathbf{S}(Q)$ and $\mathbf{v}(t)$ can be assembled as

$$\mathbf{S}(Q)=\begin{bmatrix} \mathbf{S}_1(q_1) & \mathbf{0} & \cdots & \mathbf{0} \\ \mathbf{0} & \mathbf{S}_2(q_2) & \cdots & \vdots \\ \mathbf{0} & \mathbf{0} & \cdots & \mathbf{0} \\ \mathbf{0} & \cdots & \mathbf{0} & \mathbf{S}_n(q_n) \end{bmatrix} \tag{19}$$

$$\mathbf{v}(t)=[\mathbf{v}_1\ \mathbf{v}_2\ \cdots\ \mathbf{v}_n]^T \tag{20}$$

2.4 Compliant Frame Model. As we mentioned in Sec. 1, it is difficult to model the compliant frame forces with great accuracy. However, we can approximate the forces to improve controller performance. The behavior of the compliant frame element is complicated because of the interaction of the axle modules and the nonlinear frame behavior. To simplify matters, an approximate model of the compliant frame module is developed based on the Finite Element Method (FEM) and the post-buckled frame element [5,27]. The model includes the transverse and bending forces of a compliant beam, which will be used to develop the controller in the following sections.

Given L, E, and I as the free length, Young's Modulus, and area moment of inertia of the compliant frame, respectively, the frame model is expressed in the global coordinate frame with the local coordinate definition $w_i=w_j\equiv 0$, Fig. 4, as [28]

$$\mathbf{F}_K=\mathbf{R}^T\mathbf{K}\delta_L. \tag{21}$$

Here, $\mathbf{R}$ is a rotation transformation matrix with θ defined as in Fig. 3 such that,

$$\mathbf{R}=\begin{bmatrix}\mathbf{R}_\theta & \mathbf{0}\\ \mathbf{0} & \mathbf{R}_\theta\end{bmatrix} \text{ and } \mathbf{R}_\theta=\begin{bmatrix}\cos\theta & \sin\theta & 0\\ -\sin\theta & \cos\theta & 0\\ 0 & 0 & 1\end{bmatrix}. \quad (22)$$

For convenience, δ_L is measured relative to the ith node and described as a function of the axle configuration vectors to provide,

$$\delta_L=[0\ 0\ \psi_i\ -\Delta u\ 0\ \psi_j], \quad (23)$$

where the axial deflection caused by post-buckling, Δu, is defined as $L_f-[\hat{q}_j(1)-\hat{q}_i(1)]$ and the displacements $\hat{q}_c(1)$, $c=i,j$, can be calculated from the node locations C_i and C_j by using the axle configuration vectors, q_i and q_j, expressed in the local coordinate frame as,

$$[\hat{q}_c(1)\ \hat{q}_c(2)\ \psi_c]=\mathbf{R}_\theta q_c, \quad c=i,j \quad (24)$$

The foreshortened length L_f caused by bending moments is calculated as, [29]

$$L_f=L-\Delta L=L-\frac{2\psi_i^2-\psi_i\psi_j+2\psi_j^2}{30}L. \quad (25)$$

Note that for most cases, the compliant frame of the CFMMR is not straight due to steering maneuvers [3,29], and is essentially in a post-buckled shape. So the compliant frame is deflected by axial forces as well as bending moments. Therefore the relationship between the final frame length $\hat{q}_j(1)-\hat{q}_i(1)$ and the undeformed length L is expressed as $\hat{q}_j(1)-\hat{q}_i(1)=L-\Delta L-\Delta u$, Fig. 4.

For simplicity, we use a post-buckled axial stiffness that is linear and allows for a simple solution. The axial stiffness in post-buckling is modeled as $EI\pi^2/2L^3$ [5], which is much more compliant than the traditional rigid bar model used in frame elements. Therefore, $\mathbf{K}$ is obtained as the modified post-buckling stiffness matrix where,

$$\mathbf{K}=\begin{bmatrix}\mathbf{K}_{11} & \mathbf{K}_{12}\\ \mathbf{K}_{21} & \mathbf{K}_{22}\end{bmatrix}$$

$$\mathbf{K}_{11}=\frac{EI}{L^3}\begin{bmatrix}\pi^2/2 & 0 & 0\\ 0 & 12 & 6L\\ 0 & 6L & 4L^2\end{bmatrix},\quad \mathbf{K}_{12}=\frac{EI}{L^3}\begin{bmatrix}-\pi^2/2 & 0 & 0\\ 0 & -12 & 6L\\ 0 & -6L & 4L^2\end{bmatrix}$$

$$\mathbf{K}_{21}=\mathbf{K}_{12}^T,\quad \mathbf{K}_{22}=\frac{EI}{L^3}\begin{bmatrix}\pi^2/2 & 0 & 0\\ 0 & 12 & -6L\\ 0 & -6L & 4L^2\end{bmatrix}. \quad (26)$$

3 Single Axle Nonlinear Damping Control Design

Due to the increased complexity of the system equations, the system is separated into two parts: (1) curvature-based *kinematic motion control*; and (2) robust *dynamic motion control*. Robust *dynamic motion control* is the main focus in this paper since the previously developed curvature-based *kinematic motion control* algorithms provide time-varying reference trajectories based on path state, s, and robot configuration [3,4,29]. These algorithms specify velocity trajectories for each axle to provide drift free curvature based steering algorithms for a two-axle CFMMR that minimize traction forces and account for frame foreshortening due to steering angles. Kinematic motion controllers for different configurations will be investigated in the future. The control system structure is presented in Fig. 5, which will be explained in the following subsections.

3.1 Structural Transformation of Single Axle Module. Considering the ith axle module, we rewrite the ith corresponding dynamic equation for the control design. Differentiating Eq. (13) with respect to time, substituting this result into Eq. (5), and then

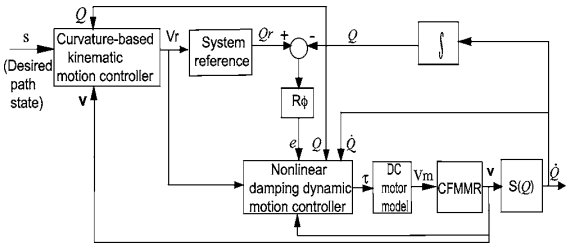

Fig. 5 A motion and dynamic control structure of the CFMMR

multiplying by $\mathbf{S}_i^{\mathbf{T}}(q_i)$, the constraint matrix $\mathbf{A}_i^T(q_i)\lambda_i$ can be eliminated. The ith axle dynamic equation of the CFMMR is then given by,

$$\mathbf{S}_i^T\mathbf{M}_i\mathbf{S}\dot{\mathbf{v}}_i+\mathbf{S}_i^T\mathbf{M}_i\dot{\mathbf{S}}\mathbf{v}_i+\mathbf{S}_i^T\mathbf{F}_i+\mathbf{S}_i^T\tau_{d,i}+\mathbf{S}_i^T\mathbf{F}_{K,i}(q_i,q_j)=\mathbf{S}_i^T\mathbf{E}_i\tau_i, \quad (27)$$

where Lagrange multipliers are no longer required and applied wheel torque is now an input to the system as a function of system states. Here we assume $\mathbf{F}_i=B_i\dot{q}_i$, where B_i consists of constant friction coefficients. The nonlinear part of the friction forces is included in $\tau_{d,i}$. Then rewrite Eq. (27) into the simplified form,

$$\bar{\mathbf{M}}_i\dot{\mathbf{v}}_i+\bar{B}_i\mathbf{v}_i+\bar{\tau}_{d,i}=\bar{\tau}_i, \quad (28)$$

where $\bar{\mathbf{M}}_i=\mathbf{S}_i^T\mathbf{M}_i\mathbf{S}_i$, $\bar{B}_i=\mathbf{S}_i^T(\mathbf{M}_i\dot{\mathbf{S}}_i+B_i\mathbf{S}_i)$, $\bar{\tau}_{d,i}=\mathbf{S}_i^T[\tau_{d,i}+\mathbf{F}_{K,i}(q_i,q_j)]$, $\bar{\tau}_i=\mathbf{S}_i^T\mathbf{E}_i\tau_i$.

The next step is to specify the dynamic extension of the velocity input, $\mathbf{v}_i\in R^{2\times 1}$, such that the regular backstepping form can be obtained:

$$\dot{q}_i=\mathbf{S}(q_i)\mathbf{v}_i \quad (29)$$

$$\bar{\mathbf{M}}_i\dot{\mathbf{v}}_i+\bar{B}_i\mathbf{v}_i+\bar{\tau}_{d,i}=\bar{\tau}_i. \quad (30)$$

These equations allow the two steering commands $\mathbf{v}_i(t)$ to be converted to desired wheel torques, $\tau_i(t)\in R^{2\times 1}$. The control objective is to derive a suitable $\tau_i(t)$ such that the CFMMR will track a specific smooth steering velocity $\mathbf{v}_{c,i}$ where,

$$\mathbf{v}_{c,i}(t)=[\nu_{c,i}\ \omega_{c,i}]^T. \quad (31)$$

This steering velocity as control input for the steering system (29) is chosen to achieve stable tracking of the reference trajectories, $q_{r,i}$. Then the CFMMR can achieve trajectory tracking given the derived wheel torques $\tau_i(t)$.

Since the reference velocity $\mathbf{v}_{r,i}$ is given by the previously mentioned motion controller, the reference trajectories $q_{r,i}$ can be solved from:

$$\dot{q}_{r,i}=S(q_{r,i})\mathbf{v}_{r,i} \quad (32)$$

Then the error state model for tracking is defined as,

$$e_i=\mathbf{R}_{\phi,i}(q_{r,i}-q_i), \quad (33)$$

where $q_{r,i}$ is the reference vector for the ith axle, $e_i\in R^{3\times 1}$ is the error position vector for the ith axle and,

$$e_i=[e_{X,i}\ e_{Y,i}\ e_{\phi,i}]^T. \quad (34)$$

As [30] shows, an alternative $\mathbf{v}_{c,i}$ is chosen as,

$$\mathbf{v}_{c,i}=\begin{bmatrix}\nu_{r,i}\cos e_{\phi,i}+k_{X,i}e_{X,i}\\ \omega_{r,i}+k_{Y,i}\nu_{r,i}e_{Y,i}+k_{\phi,i}\nu_{r,i}\sin e_{\phi,i}\end{bmatrix}, \quad (35)$$

where $k_{X,i},k_{Y,i},k_{\phi,i}$ are positive constants and $\upsilon_{r,i}$ are positive for the ith axle. The velocity control law $\mathbf{v}_{c,i}$ is thus proven [30] to make $e_i=0$ a stable equilibrium point using the Lyapunov function,

$$V_{1,i}(e_i) = \frac{1}{2}e_{X,i}^2 + \frac{1}{2}e_{Y,i}^2 + (1 - \cos e_{\phi,i})/k_{Y,i}, \tag{36}$$

and $V_{1,i}(e_i)$ is used in the subsequent controller development.

3.2 Properties and Assumptions of Single Axle Controller. There are several properties and assumptions that will be used in the following control design:

- *Assumption 1*: $\tau_{d,i}$ *and* $\mathbf{F}_{K,i}(q_i, q_j)$ *are bounded.*
- *Property 1*: $\|\bar{B}_i(q_i, \dot{q}_i)\| \leq b_i\|\dot{q}_i\| + c_i$, *where* b_i, c_i *are nonnegative constants.*
- *Property 2*: $\bar{\mathbf{M}}_i$ *is a constant matrix.*
- *Property 3*: $\dot{\mathbf{v}}_{c,i} = A_{1,i}\mathbf{v}_{c,i} + A_{2,i}\mathbf{v}_{r,i} + A_{3,i}\dot{\mathbf{v}}_{r,i}$, *where* $\|A_{1,i}\|$, $\|A_{2,i}\|$ *and* $\|A_{3,i}\|$ *are bounded.*

Proof: Properties 1 and 2 can be proven by a simple calculation, assuming the same mass of each module. Thus, we focus on the proof of Property 3.

Differentiating Eq. (35) yields,

$$\dot{\mathbf{v}}_{c,i} = \begin{bmatrix} k_{X,i}\dot{e}_{X,i} - \nu_{r,i}(\sin e_{\phi,i})\dot{e}_{\phi,i} + \dot{\nu}_{r,i}\cos e_{\phi,i} \\ \dot{\omega}_{r,i} + k_{Y,i}e_{Y,i}\dot{\nu}_{r,i} + k_{Y,i}\nu_{r,i}\dot{e}_{Y,i} + k_{\phi,i}\nu_{r,i}(\cos e_{\phi,i})\dot{e}_{\phi,i} + k_{\phi,i}\dot{\nu}_{r,i}\sin e_{\phi,i} \end{bmatrix} = \begin{bmatrix} k_{X,i} & 0 & -\nu_{r,i}(\sin e_{\phi,i}) \\ 0 & k_{Y,i}\nu_{r,i} & k_{\phi,i}\nu_{r,i}(\cos e_{\phi,i}) \end{bmatrix} \begin{bmatrix} \dot{e}_{X,i} \\ \dot{e}_{Y,i} \\ \dot{e}_{\phi,i} \end{bmatrix} + \begin{bmatrix} \cos e_{\phi,i} & 0 \\ k_{Y,i}e_{Y,i} + k_{\phi,i}\sin e_{\phi,i} & 1 \end{bmatrix} \begin{bmatrix} \dot{\nu}_{r,i} \\ \dot{\omega}_{r,i} \end{bmatrix}. \tag{37}$$

Substituting Eqs. (33) and (34) into Eq. (37) and applying Eq. (35), we can obtain,

$$\begin{aligned} \dot{\mathbf{v}}_{c,i} &= \begin{bmatrix} k_{X,i} & 0 & -\nu_{r,i}(\sin e_{\phi,i}) \\ 0 & k_{Y,i}\nu_{r,i} & k_{\phi,i}\nu_{r,i}(\cos e_{\phi,i}) \end{bmatrix} \begin{bmatrix} \omega_i e_{Y,i} - \nu_i + \nu_{r,i}\cos e_{\phi,i} \\ -\omega_i e_{X,i} + \nu_{r,i}\sin e_{\phi,i} \\ \omega_{r,i} - \omega_i \end{bmatrix} \\ &\quad + \begin{bmatrix} \cos e_{\phi,i} & 0 \\ k_{Y,i}e_{Y,i} + k_{\phi,i}\sin e_{\phi,i} & 1 \end{bmatrix} \dot{\mathbf{v}}_{r,i} \\ &= \begin{bmatrix} -k_{X,i} & k_{X,i}e_{Y,i} + \nu_{r,i}\sin e_{\phi,i} \\ 0 & -k_{Y,i}\nu_{r,i}e_{X,i} - k_{\phi,i}\nu_{r,i}\cos e_{\phi,i} \end{bmatrix} \mathbf{v}_{c,i} \\ &\quad + \begin{bmatrix} k_{X,i}\cos e_{\phi,i} & -\nu_{r,i}\sin e_{\phi,i} \\ k_{Y,i}\nu_{r,i}\sin e_{\phi,i} & k_{\phi,i}\nu_{r,i}\cos e_{\phi,i} \end{bmatrix} \mathbf{v}_{r,i} \\ &\quad + \begin{bmatrix} \cos e_{\phi,i} & 0 \\ k_{Y,i}e_{Y,i} + k_{\phi,i}\sin e_{\phi,i} & 1 \end{bmatrix} \dot{\mathbf{v}}_{r,i}. \end{aligned} \tag{38}$$

Finally, $\dot{\mathbf{v}}_{c,i}$ is simplified as,

$$\dot{\mathbf{v}}_{c,i} = A_{1,i}\mathbf{v}_{c,i} + A_{2,i}\mathbf{v}_{r,i} + A_{3,i}\dot{\mathbf{v}}_{r,i}, \tag{39}$$

where $A_{1,i}$, $A_{2,i}$, and $A_{3,i}$ are individually the coefficient matrix of $\mathbf{v}_{c,i}$, $\mathbf{v}_{r,i}$, and $\dot{\mathbf{v}}_{r,i}$.

Since $\|A_{1,i}\|$, $\|A_{2,i}\|$, and $\|A_{3,i}\|$ are checked to be bounded by inspection, Property 4 is proven. △

3.3 Nonlinear Damping Control Design of Single-Axle Module. We will now extend the nonlinear damping control scheme specified in [20] to a single-axle CFMMR configuration with time varying reference velocities.

Define the velocity error vector for each axle as,

$$\mathbf{e}_{c,i} = \begin{bmatrix} e_{v,i} \\ e_{\omega,i} \end{bmatrix} = \mathbf{v}_i - \mathbf{v}_{c,i} = \begin{bmatrix} \nu_i - \nu_{r,i}\cos e_{\phi,i} - k_{X,i}e_{X,i} \\ \omega_i - \omega_{r,i} - k_{Y,i}\nu_{r,i}e_{Y,i} - k_{\phi,i}\nu_{r,i}\sin e_{\phi,i} \end{bmatrix}. \tag{40}$$

Differentiating Eq. (40) and substituting Eq. (30) yields,

$$\bar{\mathbf{M}}_i\dot{\mathbf{e}}_{c,i} = \bar{\tau}_i - \bar{B}_i\mathbf{v}_i - \bar{\tau}_{d,i} - \bar{\mathbf{M}}_i\dot{\mathbf{v}}_{c,i}. \tag{41}$$

Then choose the Lyapunov candidate for the dynamic model, Eq. (30), as

$$V_{2,i}(\mathbf{e}_{c,i}) = \frac{1}{2}\mathbf{e}_{c,i}^T\bar{\mathbf{M}}_i\mathbf{e}_{c,i}. \tag{42}$$

Differentiating Eq. (42) yields:

$$\dot{V}_{2,i}(\mathbf{e}_{c,i}) = \mathbf{e}_{c,i}^T\bar{\mathbf{M}}_i\dot{\mathbf{e}}_{c,i} + \frac{1}{2}\mathbf{e}_{c,i}^T\dot{\bar{\mathbf{M}}}_i\mathbf{e}_{c,i}. \tag{43}$$

By substituting Eq. (41) into Eq. (43), we obtain,

$$\dot{V}_{2,i}(\mathbf{e}_{c,i}) = \mathbf{e}_{c,i}^T[\bar{\tau}_i - (\bar{B}_i\mathbf{v}_i + \bar{\mathbf{M}}_i\dot{\mathbf{v}}_{c,i} + \bar{\tau}_{d,i})] + \frac{1}{2}\mathbf{e}_{c,i}^T\dot{\bar{\mathbf{M}}}_i\mathbf{e}_{c,i}. \tag{44}$$

Applying Property 2 yields,

$$\dot{V}_{2,i}(\mathbf{e}_{c,i}) = \mathbf{e}_{c,i}^T[\bar{\tau}_i - (\bar{B}_i\mathbf{v}_i + \bar{\mathbf{M}}_i\dot{\mathbf{v}}_{c,i} + \bar{\tau}_{d,i})]. \tag{45}$$

Then applying Property 3 yields,

$$\dot{V}_{2,i}(\mathbf{e}_{c,i}) = \mathbf{e}_{c,i}^T[\bar{\tau}_i - (\bar{B}_i\mathbf{v}_i + \bar{\mathbf{M}}_iA_{1,i}\mathbf{v}_{c,i} + \bar{\mathbf{M}}_iA_{2,i}\mathbf{v}_{r,i} + \bar{\mathbf{M}}_iA_{3,i}\dot{\mathbf{v}}_{r,i} + \bar{\tau}_{d,i})]. \tag{46}$$

According to Properties 1, 3, and Assumption 1, we obtain,

$$\begin{aligned} \dot{V}_{2,i}(\mathbf{e}_{c,i}) &\leq \mathbf{e}_{c,i}^T\bar{\tau}_i + \|\mathbf{e}_{c,i}\|\{\|\bar{B}_i\|\,\|\mathbf{v}_i\| + \|\bar{\mathbf{M}}_i\|\,\|A_{1,i}\|\,\|\mathbf{v}_{c,i}\| \\ &\quad + \|\bar{\mathbf{M}}_i\|\,\|A_{2,i}\|\,\|\mathbf{v}_{r,i}\| + \|\bar{\mathbf{M}}_i\|\,\|A_{3,i}\|\,\|\dot{\mathbf{v}}_{r,i}\| + \|\bar{\tau}_{d,i}\|\} \leq \mathbf{e}_{c,i}^T\bar{\tau}_i \\ &\quad + \|\mathbf{e}_{c,i}\|\{b_i\|\mathbf{v}_i\|\,\|\mathbf{v}_i\| + c_i\|\mathbf{v}_i\| + \|\bar{\mathbf{M}}_i\|\,\|A_{1,i}\|\,\|\mathbf{v}_{c,i}\| \\ &\quad + \|\bar{\mathbf{M}}_i\|\,\|A_{2,i}\|\,\|\mathbf{v}_{r,i}\| + \|\bar{\mathbf{M}}_i\|\,\|A_{3,i}\|\,\|\dot{\mathbf{v}}_{r,i}\| + \|\tau_{d,i}\| \\ &\quad + \|\mathbf{F}_K(q_i, q_j)\|\} = \mathbf{e}_{c,i}^T\bar{\tau}_i + \|\mathbf{e}_{c,i}\|\delta_i^T\xi_i \end{aligned} \tag{47}$$

where,

$$\begin{aligned} \delta_i^T &= \{b_i, c_i, \|\bar{\mathbf{M}}_i\|\,\|A_{1,i}\|, \|\bar{\mathbf{M}}_i\|\,\|A_{2,i}\|, \|\bar{\mathbf{M}}_i\|\,\|A_{3,i}\|, \|\tau_{d,i}\|, 1\} \\ \xi_i^T &= \{\|\mathbf{v}_i\|\,\|\mathbf{v}_i\|, \|\mathbf{v}_i\|, \|\mathbf{v}_{c,i}\|, \|\mathbf{v}_{r,i}\|, \|\dot{\mathbf{v}}_{r,i}\|, 1, \|\mathbf{F}_{K,i}(q_i, q_j)\|\} \end{aligned} \tag{48}$$

Here δ_i is bounded by the above properties and assumptions, and ξ_i is a known, positive definite vector. Hence, in order to make Eq. (47) negative definite, choose,

$$\bar{\tau}_i = -K_i\mathbf{e}_{c,i}\|\xi_i\|^2, \tag{49}$$

where

$$K_i = \begin{bmatrix} K_{1,i} & 0 \\ 0 & K_{2,i} \end{bmatrix}$$

is the matrix control gain and $K_{1,i}$, $K_{2,i}$ are positive constants. The control input is then,

$$\tau_i = (\mathbf{S}_i^T \mathbf{E}_i)^{-1} \bar{\tau}_i = -(\mathbf{S}_i^T \mathbf{E}_i)^{-1} K_i \mathbf{e}_{c,i} \|\xi_i\|^2. \tag{50}$$

Substitute Eq. (49) into Eq. (47),

$$\begin{aligned} \dot{V}_{2,i}(\mathbf{e}_{c,i}) &= -\mathbf{e}_{c,i}^T K_i \mathbf{e}_{c,i} \|\xi_i\|^2 + \|\mathbf{e}_{c,i}\| \delta_i^T \xi_i \\ &\leqslant -\|K_i\| \|\mathbf{e}_{c,i}\|^2 \|\xi_i\|^2 + \|\mathbf{e}_{c,i}\| \|\delta_i\| \|\xi_i\| \\ &= -\|K_i\| \left\{ \|\mathbf{e}_{c,i}\| \|\xi_i\| - \frac{\|\delta_i\|}{2\|K_i\|} \right\}^2 + \frac{\|\delta_i\|^2}{4\|K_i\|} \end{aligned} \tag{51}$$

By using the Lyapunov function $V_i = V_{1,i} + V_{2,i}$ [20,31], $\mathbb{C}_i = [\mathbf{e}_i \ \mathbf{e}_{c,i}]^T$ is globally uniformly bounded and the velocity tracking error becomes arbitrarily small by increasing the control gain K_i.

Note that the reference velocity vector is included in the control input since the motion controller could provide time varying reference velocities. The compliant frame force $\mathbf{F}_{K,i}(q_i, q_j)$ is also taken consideration in the controller, which is the topic of the next subsection.

3.4 Compliant Frame Effect on Control Design. There are two cases to consider for the CFMMR in terms of the compliant frame effect on control design. On one hand, the approximate model of the compliant frame force, $\mathbf{F}_{K,i}(q_i, q_j)$, may be used and the inaccurate part of this model will become part of the disturbance, $\tau_{d,i}$, and δ_i and ξ_i are chosen per Eq. (48). On the other hand, $\mathbf{F}_{K,i}(q_i, q_j)$ may be considered to be totally unknown and δ_i and ξ_i will be redefined as

$$\delta_i^T = \{b_i, c_i, \|\bar{\mathbf{M}}_i\| \|A_{1,i}\|, \|\bar{\mathbf{M}}_i\| \|A_{2,i}\|, \|\bar{\mathbf{M}}_i\| \|A_{3,i}\|, \|\tau_{d,i} + \mathbf{F}_{K,i}(q_i, q_j)\|\}$$

$$\xi_i^T = \{\|\mathbf{v}_i\| \|\mathbf{v}_i\|, \|\mathbf{v}_i\|, \|\mathbf{v}_{c,i}\|, \|\mathbf{v}_{r,i}\|, \|\dot{\mathbf{v}}_{r,i}\|, 1\} \tag{52}$$

which helps to decrease computational requirements since $\mathbf{F}_{K,i}(q_i, q_j)$ is not calculated between time steps.

We will apply both control inputs determined by Eqs. (48) and (52) to the experimental platform and compare them in Sec. 5 in order to determine the characteristics of performance, tracking errors, and computations.

4 Multi-axle Distributed Control Design

The distributed controller is designed for a multiaxle CFMMR based on the above single-axle controller. That is to say, the distributed controller is composed of n independent controllers $\tau_j, j = 1 \sim n$ as:

$$\tau_j = -(\mathbf{S}_j^T \mathbf{E}_j)^{-1} K_j \mathbf{e}_{c,j} \|\xi_j\|^2. \tag{53}$$

Proposition: The multiaxle CFMMR can achieve stable trajectory tracking with the distributed controller (53) *if the response of each module is globally uniformly bounded by its corresponding single-axle controller.*

Proof: Choose the composite Lyapunov function candidate,

$$V = V_1 + \ldots + V_i + \ldots + V_n = V_{1,1} + V_{2,1} + \ldots + V_{1,i} + V_{2,i} + \ldots + V_{1,n} + V_{2,n}. \tag{54}$$

Substituting Eqs. (36) and (42) into Eq. (54) produces,

$$\begin{aligned} V = &\frac{1}{2} e_{X,1}^2 + \frac{1}{2} e_{Y,1}^2 + (1 - \cos e_{\phi,1})/k_{Y,1} + \frac{1}{2} \mathbf{e}_{c,1}^T \bar{\mathbf{M}}_1 \mathbf{e}_{c,1} + \ldots + \frac{1}{2} e_{X,i}^2 \\ &+ \frac{1}{2} e_{Y,i}^2 + (1 - \cos e_{\phi,i})/k_{Y,i} + \frac{1}{2} \mathbf{e}_{c,i}^T \bar{\mathbf{M}}_i \mathbf{e}_{c,i} + \ldots + \frac{1}{2} e_{X,n}^2 + \frac{1}{2} e_{Y,n}^2 \\ &+ (1 - \cos e_{\phi,n})/k_{Y,n} + \frac{1}{2} \mathbf{e}_{c,n}^T \bar{\mathbf{M}}_n \mathbf{e}_{c,n}. \end{aligned} \tag{55}$$

Differentiating Eq. (55) and applying Eqs. (33) and (51) yields,

$$\begin{aligned} \dot{V} \leqslant &-k_{X,1} e_{X,1}^2 - \frac{k_{\phi,1}}{k_{Y,1}} \nu_{r,1} \sin^2 e_{\phi,1} - \|K_1\| \left\{ \|\mathbf{e}_{c,1}\| \|\xi_1\| - \frac{\|\delta_1\|}{2\|K_1\|} \right\}^2 \\ &+ \frac{\|\delta_1\|^2}{4\|K_1\|} - \ldots - k_{X,i} e_{X,i}^2 - \frac{k_{\phi,i}}{k_{Y,i}} \nu_{r,i} \sin^2 e_{\phi,i} - \|K_i\| \left\{ \|\mathbf{e}_{c,i}\| \|\xi_i\| \right. \\ &\left. - \frac{\|\delta_i\|}{2\|K_i\|} \right\}^2 + \frac{\|\delta_i\|^2}{4\|K_i\|} - \ldots - k_{X,n} e_{X,n}^2 - \frac{k_{\phi,n}}{k_{Y,n}} \nu_{r,n} \sin^2 e_{\phi,n} - \|K_n\| \\ &\times \left\{ \|\mathbf{e}_{c,n}\| \|\xi_n\| - \frac{\|\delta_n\|}{2\|K_n\|} \right\}^2 + \frac{\|\delta_n\|^2}{4\|K_n\|}, \end{aligned} \tag{56}$$

where $K_1, \ldots, K_n$ are positive definite matrices, $k_{X,1}, \ldots, k_{X,n}, k_{Y,1}, \ldots, k_{Y,n}, k_{\phi,1}, \ldots, k_{\phi,n}$ are positive constants, and $\|\delta_1\|, \ldots, \|\delta_n\|$ are bounded. Therefore,

$$\begin{aligned} \dot{V} &\leqslant -k_{X,1} e_{X,1}^2 - \frac{k_{\phi,1}}{k_{Y,1}} \nu_{r,1} \sin^2 e_{\phi,1} - \ldots - k_{X,i} e_{X,i}^2 - \frac{k_{\phi,i}}{k_{Y,i}} \nu_{r,i} \sin^2 e_{\phi,i} \\ &\quad - \ldots - k_{X,n} e_{X,n}^2 - \frac{k_{\phi,n}}{k_{Y,n}} \nu_{r,n} \sin^2 e_{\phi,n} \\ &= -W(\mathbf{e}), \end{aligned} \tag{57}$$

when,

$$\|\mathbf{e}_{c,1}\| \geqslant \frac{1}{\|K_1\|} \frac{\|\delta_1\|}{\|\xi_1\|}, \ldots, \|\mathbf{e}_{c,n}\| \geqslant \frac{1}{\|K_n\|} \frac{\|\delta_n\|}{\|\xi_n\|}, \tag{58}$$

where $\mathbf{e} = [\mathbb{C}_1 \ \ldots \ \mathbb{C}_n]^T$, $\mathbb{C}_j = [\mathbf{e}_j \ \mathbf{e}_{c,j}]^T$, $j = 1 \sim n$, and $W(\mathbf{e})$ is a continuous positive definite function.

Hence we conclude that $\mathbf{e}$ is globally uniformly bounded [31]. According to Eq. (58), the tracking error bounds of each module becomes smaller as the norm of the corresponding control gain matrix, K_i, is increased. However, tracking error bound for the multiaxle CFMMR becomes more complicated. The modules are interconnected by compliant frames, so the behavior of each module can affect the others. Increasing the control gain for one axle may increase the tracking error of another. Second, the tracking error bounds are increased as the term δ_i increases, which may be caused by increased disturbances or model uncertainty. Therefore it is proper to minimize the tracking errors for the entire system by experimentally tuning the set of control gains, $K_1, \ldots, K_n$. Δ

5 Controller Evaluation

5.1 Methods and Procedures. The distributed nonlinear damping controller for the two-axle CFMMR was simulated in MATLAB® and SIMULINK®. The reference velocities $\mathbf{v}_r$ of both axles are generated by a drift-free curvature-based *kinematic motion control* algorithm guiding midpoint, O, of the robot to follow the desired path [4,26]. The velocity trajectories are specified for each axle such that the distance between points C_1 and C_2 remains consistent with the ideal foreshortened length, L_f, of the frame given the current axle headings [29]. As we mentioned in Sec. 4, the control gains need to be tuned to minimize the tracking error bounds. The gains were first tuned in simulation until the tracking errors were within 10^{-3} with a similar time step size, 10^{-3}. These gains were then verified in experiment.

Several experiments were conducted on a two-module CFMMR

Table 1 Prototype of a two-module CFMMR

Parameter	Value	Units	Description
r_w	0.073	Meters	Wheel radius
d	0.162	Meters	Axle width (half)
m_i	4.76	Kg	Mass of each axle
J_i	0.0186	Kg/m^2	Mass moment of inertia of each axle

Table 2 Parameters of compliant frame

Parameter	Value	Units	Descriptions
L	0.37	meters	Length
w	0.05	meters	Width
t	0.7	mm	Thickness
E	2.0×10^{11}	Pa	Young's modulus
A	3.5×10^{-5}	m^2	Cross-sectional area
ρ	7.8×10^{3}	Kg/m^3	Density
I	1.4292×10^{-12}	m^4	Area moment of inertia

Table 3 Initial positions of three different shapes.

Path	x	y	ϕ
Line	−0.1	0.1	0
Circle	1.05	−0.2	$\pi/2$
Sine wave	−0.09	−0.04	$\pi/4$

experimental platform, Fig. 1, at the University of Utah. The robot is controlled via tether by a dSpace™ 1103 DSP board and an external power supply. Each wheel is actuated by a geared dc motor with voltage input V_m, Fig. 5. The real-time position of each wheel is detected by an encoder and odometry is used for predicting the axle posture. Video is used to illustrate the robot performance. Here we apply controllers with and without beam force compensation to consider their effect on performance.

The prototype parameters, Table 1, and the parameters of the compliant frame, Table 2, are used for both simulations and experiments. Three different path shapes, a straight line, a circle, and a sine wave were used with nonzero initial positions of midpoint O, Table 3. The straight line is the simplest path, where the reference is only a constant linear velocity. The circle is more complicated since the reference is ultimately constant linear and angular velocities. The sine wave is the most complicated, since the path consists of time varying linear and angular velocities. Therefore, the tracking performance of the robot can be evaluated comprehensively.

5.2 Results. Using the tuned gains

$$K_1 = K_2 = \begin{bmatrix} 30 & 0 \\ 0 & 5 \end{bmatrix},$$

the simulation results predict that the robot follows the corresponding desired paths perfectly. Experimental odometry results corroborate the simulated results well, except for some chattering and apparent wheel slippage.

Figure 6 shows the experimental posture data (according to

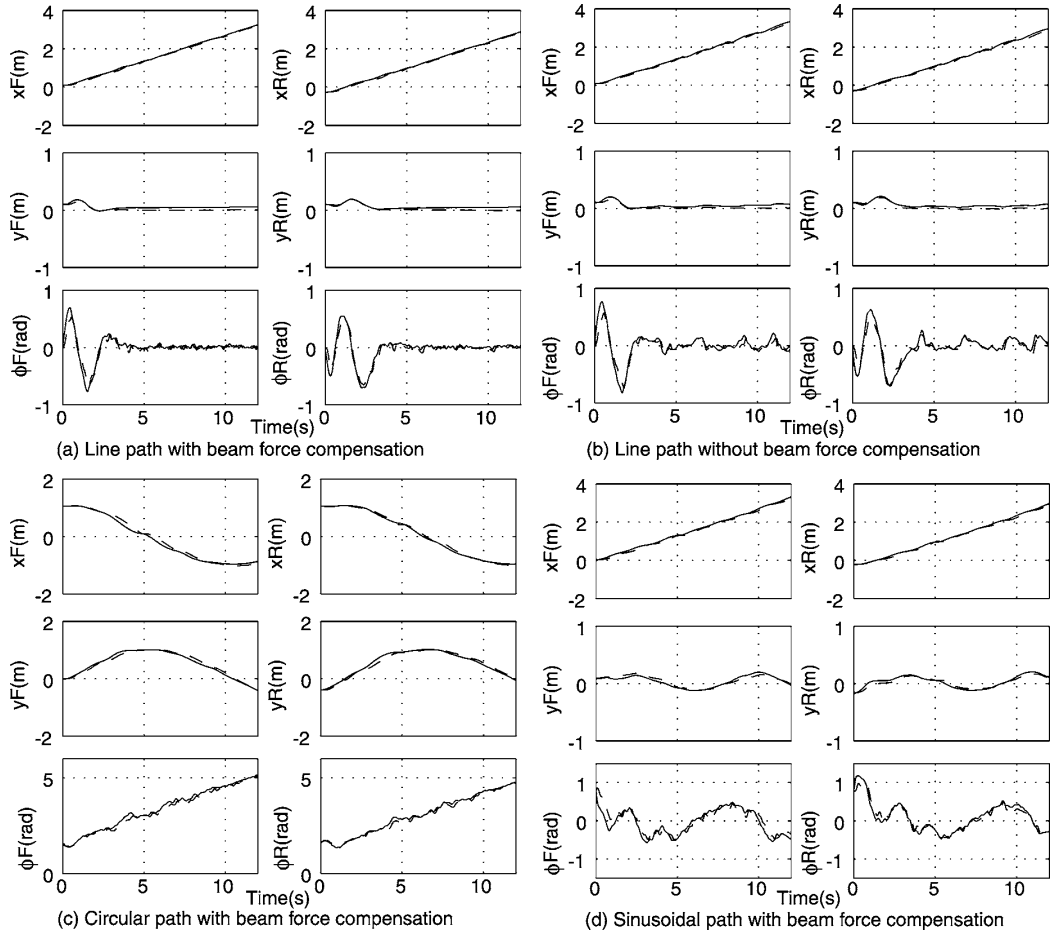

Fig. 6 Experimental posture data for path following, where solid lines represent the desired position and dashed lines represent the experimentally determined position

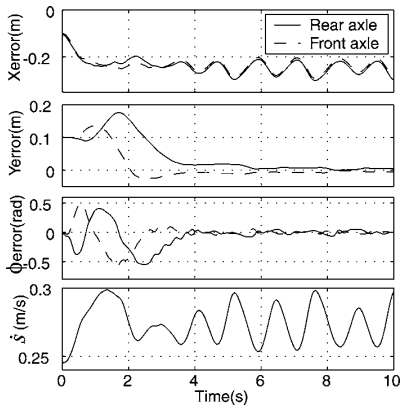

Fig. 7 Experimental position errors of each axle and reference velocity of middle point *O* while line path following according to odometric data

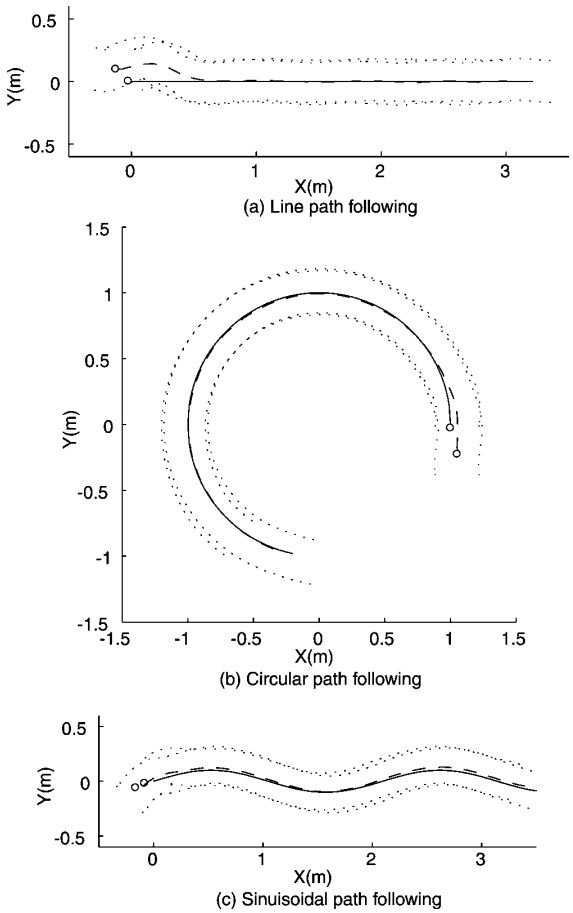

Fig. 8 Experimental path following results without beam force compensation according to odometric data

odometry) of the path following both with and without beam force compensation. The desired position is represented by the solid lines and the experimentally determined position is represented by the dashed lines. Figure 7 shows the position errors of each axle and the reference velocity, $\dot{s}$, of the midpoint O, where the position error of the rear axle is represented by the solid line and the position error of the front axle is represented by the dashed line. Figure 8 shows the experimental path following results without beam force compensation, where the desired trajectory of the midpoint, O, of the robot is represented by the solid line, the experimental trajectory of the midpoint, O, is represented by the dashed line, and the trajectory of the wheels are represented by dotted lines. Figure 9 shows the snapshots of the video for the line path following. The dotted lines are from simulation results, which represent the path of the midpoint O and each wheel, respectively. The white line illustrates the actual path that the robot converges to, which is parallel to the desired path (along the x axis), but offset by −0.06 m. Note that according to odometry, however, the robot converges to the specified paths quite well, Fig. 6. All of these results were conducted with the robot on a smooth, flat, high traction carpet surface.

5.3 Discussion. As Fig. 6 indicates, the system performed well while following the paths; even with nonzero initial error states and uncertain disturbance due to model inaccuracy. Note that compared with the pure model-based backstepping controller presented in [5], the nonlinear damping controller derived here compensates model uncertainty and does not need to adjust the control gains during the experiments. Thus, once the control gains are tuned properly in simulation, they can be used in experiment directly without off-tracking, as witnessed in previous results. This critical characteristic demonstrates the robustness of the controller applied to groups of axle modules bound by uncertain interaction forces.

As Figs. 6(*a*) and 6(*b*) indicate, while the line path following the controller with beam force compensation can achieve tighter performance and less tracking error, but more computation is required to predict those forces. The controller without beam force compensation is less aggressive at the cost of increasing the tracking error slightly. Both of them work well with the two-axle CFMMR. However, as the configuration and the environment become more and more complicated, the compliant frame forces will play more important roles in the robot performance. The controller with beam force compensation will be preferable, even though more computation will be required. Therefore, in the near future, the controller with beam force compensation will be used for the two-axle CFMMR on the rough terrain, such as on sand or with scattered rocks. Additional relative position sensors will then be introduced to help measure the relative position between the adjacent modules and predict the compliant frame forces more accurately.

As Fig. 7 indicates, the actual X position lags the reference position and oscillates. The Y position errors converge to a small value close to zero. The ϕ errors converge well except for a small chattering. Note that the reference velocity, $\dot{s}$, of the middle point O has oscillations that causes the oscillation of X position errors. These oscillations also cause, in part, the saturation of the wheel torques, Fig. 10, which will be discussed later. In the design of curvature-based *kinematic motion controller*, a positive constant ε was introduced to make this controller smooth. This introduction of ε causes the lagged X position, however. Improving the *kinematic motion control* to solve the lag problem is a subject of future work.

The 0.06 m-odometry error is observed in Fig. 9, which is mainly caused by wheel slippage. The apparent wheel slippage occurred in the first second because of the fast maneuvering turn of the robot. The torque saturation was also observed in the experiments, see Figs. 10(*d*). First, the saturation is caused by phase lag in the odometry measurement system. In the odometry system, second-order filters are used to decrease measurement noise. The filter also increases phase lag and makes the system closer to marginal stability. In this case, the filter was chosen to reduce the

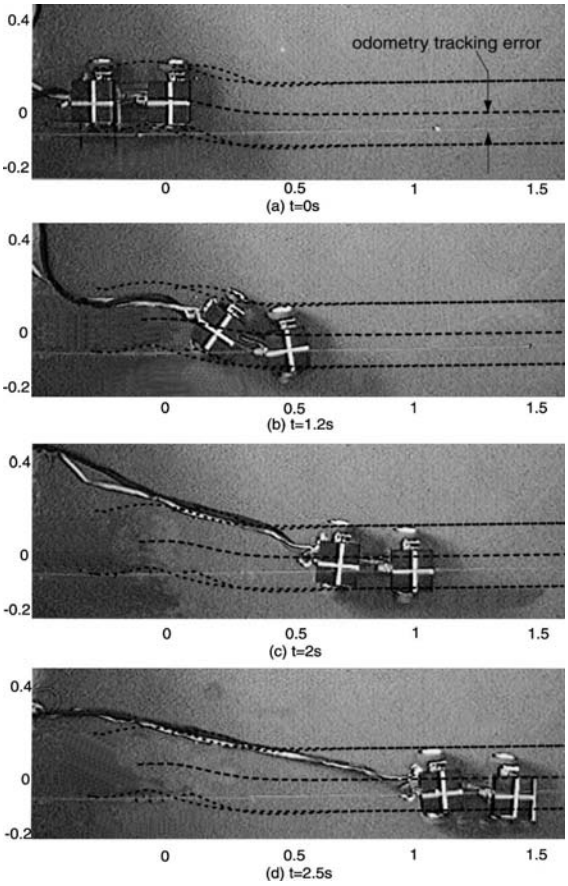

Fig. 9 Snapshots of line path following without beam compensation

noise, but introduced the corresponding oscillations and aggravated saturation. Additional sensor fusion algorithms will be used to reduce the odometry problems in the near future.

As Fig. 10 indicates, unmodeled uncertainties of the robot also contribute to torque saturation. In order to evaluate this problem, a series of line path following experiments were performed on surfaces with increasing traction characteristics, such as no ground contact, on sand, and on carpet. In the case of no ground contact, the robot was put on a box so that all the wheels are free to rotate without any surface interaction. It was used to narrow down the possible causes of torque saturation. Figure 10(*a*) shows the simulation results of the wheel torques. Figures 10(*b*)–10(*d*) show the experimental results in the three mentioned conditions. The average percent saturation for all the wheels in each case is investigated as well, Table 4. As Fig. 10 and Table 4 show, (*b*)–(*d*) have saturation that does not appear in simulation, which predicts that the unmodeled plant characteristics (such as backlash, unmodeled frame forces, friction, etc.) cause the saturation. Comparing (*c*) and (*d*) with (*b*), note that (*b*) has the least uncertainties caused by

Table 4 Analysis data of average torque saturation

Condition	In simulation	No ground contact	On sand	On carpet
Saturation percentage	0	19	28	32

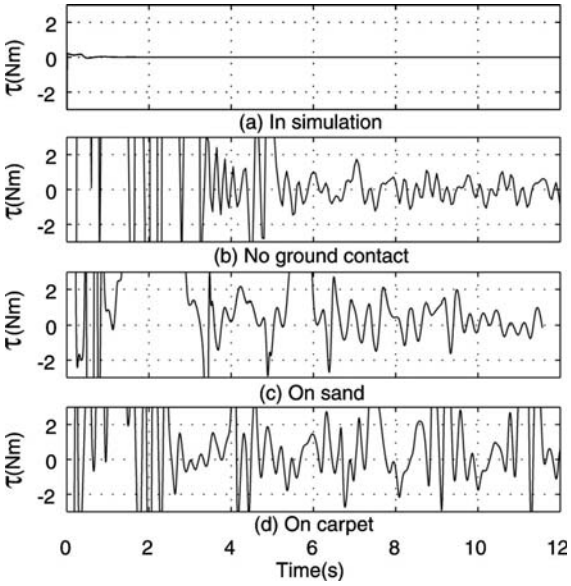

Fig. 10 Experimental and simulation results illustrating torque saturation of the front left wheel while line path following

the flexible frame and friction, and, therefore, has the least saturation. Comparing (*b*) and (*c*) with (*d*), note that (*d*) has the highest traction on carpet, and therefore has the most saturation. Hence, the torque saturation increases as the number of uncertainties of the robot increases. Hence, it is concluded that torque saturation is caused, in part, by model uncertainty.

6 Conclusions

In this paper we introduce a distributed nonlinear damping controller for dynamic motion control of wheeled Compliant Framed Modular Mobile Robots to compensate for model uncertainty with unknown bounds. Simulation and experimental results for a two-axle CFMMR configuration demonstrate the robustness of the proposed controller. This control algorithm is generally applicable to other mobile robots, which have unknown or partially known uncertainties. Future work will focus on improving the kinematic motion control, additional sensor algorithms incorporating relative position sensors, and the behavior of the CFMMR on the rough terrain.

Acknowledgment

The authors gratefully acknowledge support of this research provided by NSF Grant No. IIS-0308056.

References

[1] Yim, M., Roufas, K., Duff, D., Zhang, Y., Eldershaw, C., and Homans, S., 2003, "Modular Reconfigurable Robots in Space Applications," Auton. Rob., **14**, pp. 225–237.
[2] Ambrose, R. O., Aalund, M. P., and Tesar, D., 1993, "Designing Modular Robots for a Spectrum of Space Applications," in *Cooperative Intelligent Robotics in Space III*, 16–18 Nov 1992, Boston, MA, pp. 371–381.
[3] Albiston, B. W., and Minor, M. A., 2003, "Curvature Based Point Stabilization for Compliant Framed Wheeled Modular Mobile Robots," in *IEEE ICRA*, 14–19 Sep 2003, Taipei, Taiwan, pp. 83–89.
[4] Albiston, B. W., 2003, "Curvature Based Point Stabilization and Path Following for Compliant Framed Wheeled Modular Mobile Robots," Masters Thesis, University of Utah, Salt Lake City, UT, 92 pp.
[5] Park, S., and Minor, M. A., 2004, "Modeling and Dynamic Control of Compliant Framed Wheeled Modular Mobile Robots," in *IEEE ICRA*, Apr 26–May 1 2004, New Orleans, LA, pp. 3937–3943.
[6] Merrell, R., and Minor, M. A., 2003, "Internal Posture Sensing for a Flexible Frame Modular Mobile Robot," in *IEEE ICRA*, 14–19 Sep 2003, Taipei, Tai-

wan, pp. 452–457.
[7] Bekker, M. G., 1962, "Vehicle With Flexible Frame," U.S. Patent 3235020.
[8] Borenstein, J., 1995, "Control and Kinematic Design of Multi-Degree-of-Freedom Mobile Robots With Compliant Linkage," IEEE Trans. Rob. Autom., **11**, pp. 21–35.
[9] Mori, M., and Hirose, S., 2002, "Three-Dimensional Serpentine Motion and Lateral Rolling by Active Cord Mechanism ACM-R3," in *Proc. 2002 IEEE/RSJ Int'l Conf. Intel. Rob. and Sys. (IROS '02)*, 30 Sep–4 Oct, Lausanne, Switzerland, pp. 829–834.
[10] Kamegawa, T., Yamasaki, T., Igarashi, H., and Matsuno, F., 2004, "Development of the Snake-Like Rescue Robot KOHGA," in *Proc. 2004 IEEE Int'l Conf. on Rob. and Autom.*, 26 Apr–1 May, New Orleans, LA, pp. 5081–5086.
[11] Klaassen, B., and Paap, K. L., 1999, "GMD-SNAKE2: A Snake-Like Robot Driven by Wheels and a Method for Motion Control," *Proc. 1999 IEEE Int'l Conf. on Rob. and Autom., ICRA99*, Detroit, MI, 10–15 May, Vol. 4, pp. 3014–3019.
[12] Kimura, H., and Hirose, S., 2002, "Development of Genbu: Active Wheel Passive Joint Articulated Mobile Robot," in *2002 IEEE/RSJ Int'l Conf. on Intel. Rob. and Sys.(IROS 02)*, 30 Sep–4 Oct, Lausanne, Switzerland, pp. 823–828.
[13] Cheong, J., Chung, W. K., and Youm, Y., 2002, "PID Composite Controller and its Tuning for Flexible Link Robots," in *IEEE/RSJ Int. Conf. on Intelligent Robots and Systems*, 30 Sep–4 Oct 2002, Lausanne, Switzerland, pp. 2122–2127.
[14] Wang, X., and Mills, J. K., 2004, "A FEM Model for Active Vibration Control of Flexible Linkages," in *Proc.-IEEE ICRA*, 26 Apr–1 May 2004, New Orleans, LA, pp. 4308–4313.
[15] Hirata, Y., Kume, Y., Sawada, T., Wang, Z.-D., and Kosuge, K., 2004, "Handling of an Object by Multiple Mobile Manipulators in Coordination Based on Caster-Like Dynamics," in *2004 IEEE ICRA*, 26 Apr–1 May 2004, New Orleans, LA, pp. 807–812.
[16] Tang, C. P., Bhatt, R., and Krovi, V., 2004, "Decentralized Kinematic Control of Payload Transport by a System of Mobile Manipulators," in *2004 IEEE ICRA*, 26 Apr–1 May 2004, New Orleans, LA, pp. 2462–2467.
[17] Tayebi, A., Tadjine, M., and Rachid, A., 1997, "Invariant Manifold Approach for the Stabilization of Nonholonomic Systems in Chained Form: Application to a Car-Like Mobile Robot," in *Proc. of the 1997 36th IEEE Conf. on Decision and Control*, Part 4 (of 5), 10–12 December 1997, San Diego, CA, pp. 4038–4043.
[18] Fierro, R., and Lewis, F. L., 1997, "Control of a Nonholonomic Mobile Robot: Backstepping Kinematics Into Dynamics," J. Rob. Syst., **14**, pp. 149–163.
[19] Yang, J.-M., and Kim, J.-H., 1999, "Sliding Mode Motion Control of Nonholonomic Mobile Robots," IEEE Trans. Control Syst. Technol., **19**, pp. 15–23.
[20] Lin, S., and Goldenberg, A., 2000, "Robust Damping Control of Wheeled Mobile Robots," in *ICRA 2000*, 24–28 Apr 2000, San Francisco, CA, pp. 2919–2924.
[21] Wang, Z. P., Ge, S. S., and Lee, T. H., 2004, "Robust Motion/Force Control of Uncertain Holonomic/Nonholonomic Mechanical Systems," *IEEE/ASME Transactions on Mechatronics*, **9**, pp. 118–123.
[22] Wilson, D. G., and Robinett, III, R. D., 2001, "Robust Adaptive Backstepping Control for a Nonholonomic Mobile Robot," in *IEEE Int. Conf. on Systems, Man and Cybernetics*, 7–10 Oct 2001, Tucson, AZ, pp. 3241–3245.
[23] Kim, M. S., Shin, J. H., and Lee, J. J., 2000, "Design of a Robust Adaptive Controller for a Mobile Robot," in *IEEE/RSJ International Conference on Intelligent Robots and Systems*, 31 Oct–5 Nov 2000, Takamatsu, pp. 1816–1820.
[24] Fierro, R., and Lewis, F. L., 1998, "Control of a Nonholonomic Mobile Robot Using Neural Networks," IEEE Trans. Neural Netw., **9**, pp. 589–600.
[25] Fierro, R., and Lewis, F. L., 1996, "Practical Point Stabilization of a Nonholonomic Mobile Robot Using Neural Networks," in *Proceedings of the 1996 35th IEEE Conference on Decision and Control*, 11–13 Dec 1996, Kobe, Japan, pp. 1722–1727.
[26] Tayebi, A., and Rachid, A., 1997, "A Unified Discontinuous State Feedback Controller for the Path-Following and the Point-Stabilization Problems of a Unicycle-Like Mobile Robot," in *Proc. of the 1997 IEEE Int. Conf. on Control Applications*, Hartford, CT, pp. 31–35.
[27] Park, S., 2004, "Modeling and Dynamic Control for Compliant Framed Wheeled Modular Mobile Robots," in *Mechanical Engineering*, Salt Lake City, University of Utah.
[28] Spanski, P. L., 1970, "Flexible Frame Vehicle," U.S. Patent 3550710.
[29] Minor, M. A., Albiston, B., and Schwensen, C., 2006, "Simplified Motion Control of a Two-Axle Compliant Framed Wheeled Mobile Robot," IEEE Trans. Rob. Autom., **22**, pp. 491–506.
[30] Kanayama, Y., Kimura, Y., Miyazaki, F., and Noguchi, T., 1990, "A Stable Tracking Control Method for an Autonomous Mobile Robot," in *1990 IEEE ICRA*, 13–18 May 1990, Cincinnati, OH, pp. 384–389.
[31] Khalil, H., 2002, *Nonlinear Systems*, 3rd ed., Prentice–Hall, Upper Saddle River, NJ.

CHAPTER 3

COOPERATIVE MOTION CONTROL AND SENSING ARCHITECTURE

This chapter is a journal paper conditionally accepted by the IEEE Transactions on Robotics. Authors are Xiaorui Zhu, Youngshik Kim, Roy Merrell, and Mark A. Minor.

3.1 Abstract

A novel motion control and sensing architecture for a two-axle Compliant Framed wheeled Modular Mobile Robot (CFMMR) is proposed in this paper. The CFMMR is essentially a cooperative mobile robotic system with complex physical constraints and highly nonlinear interaction forces. The architecture combines a kinematic controller for coordinating motion and providing reference commands, robust dynamic controllers for following these commands and rejecting disturbances, and a sensor fusion system designed to provide accurate relative posture estimates. Requirements for each of these subsystems and their respective interconnections are defined in this paper in order to optimize system performance. Experimental results compare performance of the proposed architecture to suboptimal configurations. Results derived from seven groups of experiments based upon 35 individual tests validate superiority of the architecture.

Index Terms: Motion control, Robot sensing systems, Cooperative systems, Distributed control, Tracking.

3.2 Introduction

Cooperative motion control and sensing for Compliant Framed wheeled Modular Mobile Robots (CFMMR), Figure 3.1, is the focus of this research. The CFMMR uses compliant frame members to couple rigid axle modules with independently controlled wheels [1]. Wheel commands are used to deform the frame for advanced steering capability. Frame compliance also allows the robot to twist its shape and adapt to rugged terrain. Simplicity and modularity of the system emphasize its cost effectiveness, durability in adverse climates, and capability to be reconfigured for a multitude of applications.

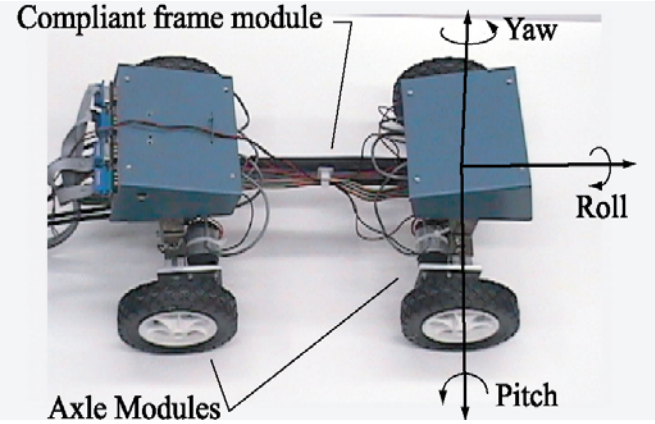

Figure 3.1. Two-axle CFMMR experimental configuration.

A number of cooperative wheeled mobile robots have been investigated in recent decades. A detailed comparison is described in [1, 2]. Most similar of these is the snake-like robot Genbu [3], which uses entirely passive joints to allow cooperation amongst wheel axles for adaptation to uneven terrain. However, motion control of [3] focused on the simple posture alignment and functional ability [3, 4] while this paper deals with general navigation issues and accurate motion control.

In this paper, we propose a new sensing and control architecture in order for the system to be scalable, distributed, and cooperative. The architecture, Figure 3.2, consists

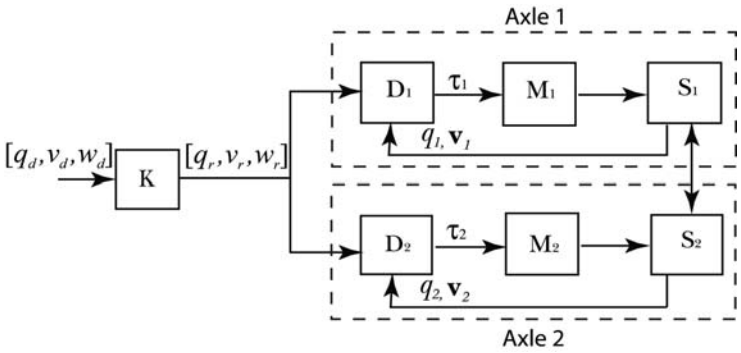

Figure 3.2. Distributed sensing and control configurations where K represents kinematic motion control, D represents dynamic motion control, S represents sensory system, and M represents each module of the robot.

of kinematic (K) control, dynamic (D) control, and sensing (S) systems components. In this architecture, each axle module is treated individually as an autonomous mobile robot unit. Thus, identical algorithms can be applied to each unit of the system, which provides naturally distributed computational burden. Compliant coupling complicates this task, however, since each axle imposes boundary conditions on its neighboring compliant frame elements and resulting interaction forces are created.

In order to reduce interaction forces in lieu of nonholonomic constraints, axle cooperation is managed via centralized kinematic control. Based on ideal kinematics, the kinematic controller considers frame boundary conditions and provides bounded posture and velocity commands such that the system follows a reference trajectory or regulates to a final posture asymptotically. The distributed dynamic controllers then track these reference commands such that physical constraints are satisfied during movement of the robot in lieu of disturbances. Since off-tracking between neighboring axles can increase interaction forces, the distributed sensing system includes a relative position sensor within a tiered fusion algorithm to provide accurate posture and velocity estimates.

Motion control of wheeled mobile robots has received appreciable attention in recent years, where rigid axle wheeled mobile robots are predominant platforms. In earlier stages, most research was based on the kinematic model of a wheeled mobile robot where the input is velocity [5, 6]. However, tracking the velocity commands with an actual robot and rejecting the resulting drift is not trivial. Thus, the uniform dynamic controllers derived in [7, 8] were based on the kinematic and dynamic model of the robot such that the robot can be controlled using wheel torque commands. Motion control of the CFMMR, however, is different in two aspects. First, the physical constraints,

especially the axle velocity and curvature constraints imposed by the frame, are not typical in rigid body wheeled mobile robots that are the focus of the uniform dynamic controllers. Second, the interaction forces between the axles are highly nonlinear functions of relative axle postures. Thus, coordinating relative axle postures is a critical concern that is not considered by the uniform dynamic controllers mentioned above. In contrast, the motion control architecture proposed here is ideal for coordinating motion of the axles in lieu of interaction constraints.

Coordination is a common issue in cooperative mobile robotics, and has been considered with a variety of techniques [9-14]. Some of them only focus on motion planning and coordination issues without sensor architecture involved [11, 14]. Some only consider motion planning and sensor architecture ignoring robot dynamics [9, 13]. Others only focus on dynamic motion control and coordinated force control without considering motion planning and sensor issues [10, 12, 15]. None of them consider the combination of motion planning, dynamic motion control and complex sensor fusion. There is no general solution to resolve all three aspects. In reality, motion planning, dynamic control and sensor architecture issue, however, all affect efficiency of cooperative motion control.

Burdick and his students proposed controllability and motion planning issues for multimodel systems including over-constrained wheeled vehicles where conventional nonholonomic motion planning and control theories do not apply [16]. They developed a power dissipation method (PDM) and talked about the conditions of kinematic reducibility for such systems. Then the solutions of PDM were shown actually as the solutions of kinematic reducibility. The PDM technique was provided to simplify motion

control analysis from the full Lagrangian mechanical framework. As they stated, however, the full Lagrangian still plays an important role in analyzing mechanical systems in general. While the CFMMR has similarities to over-constrained wheeled vehicles, this paper provides a motion control and sensing architecture based on the general full Lagrangian analysis to accommodate the conventional nonholonomic control theories onto the cooperative nonholonomic system.

The main contributions of this paper involve a distributed cooperative motion control and sensing architecture. The architecture and requirements for the kinematic controller, dynamic controller, and sensor system components are specified in order to reduce tracking error in lieu of robot interaction forces and unmodeled disturbances. The architecture provides a framework optimized for allowing previous research on the aforementioned topics to be combined to form a robust cooperative motion control system [2, 17, 18]. Therefore, algorithms and controllers previously developed for each component are implemented and the architecture is evaluated experimentally. While the target application is the CFMMR, this architecture is easily extended to any cooperative mobile robotic system, but the specific algorithms in the modules may need to be customized for a particular application. Further, given the modular structure of the architecture, it is easy to customize specific components to satisfy navigation requirements of the robot and to allow a team to design the components in parallel for faster implementation.

The structure of the paper follows. The generic modeling structure is presented in Section 3.3 as a foundation for sensing and control. Our overall motion control and sensing strategy is discussed for a two-axle CFMMR in Section 3.4. The requirements

and implementation of the kinematic motion controller, the dynamic motion controller and the sensory system are presented in Sections 3.5-3.7. The experimental evaluation is discussed in Section 3.8. Concluding remarks and future works are described in Section 3.9.

3.3 Generic Modeling Structure

Consider the CFMMR model shown in Figure 3.3, which shows two axles connected by a compliant frame member. Based on a one-axle unicycle-type wheeled

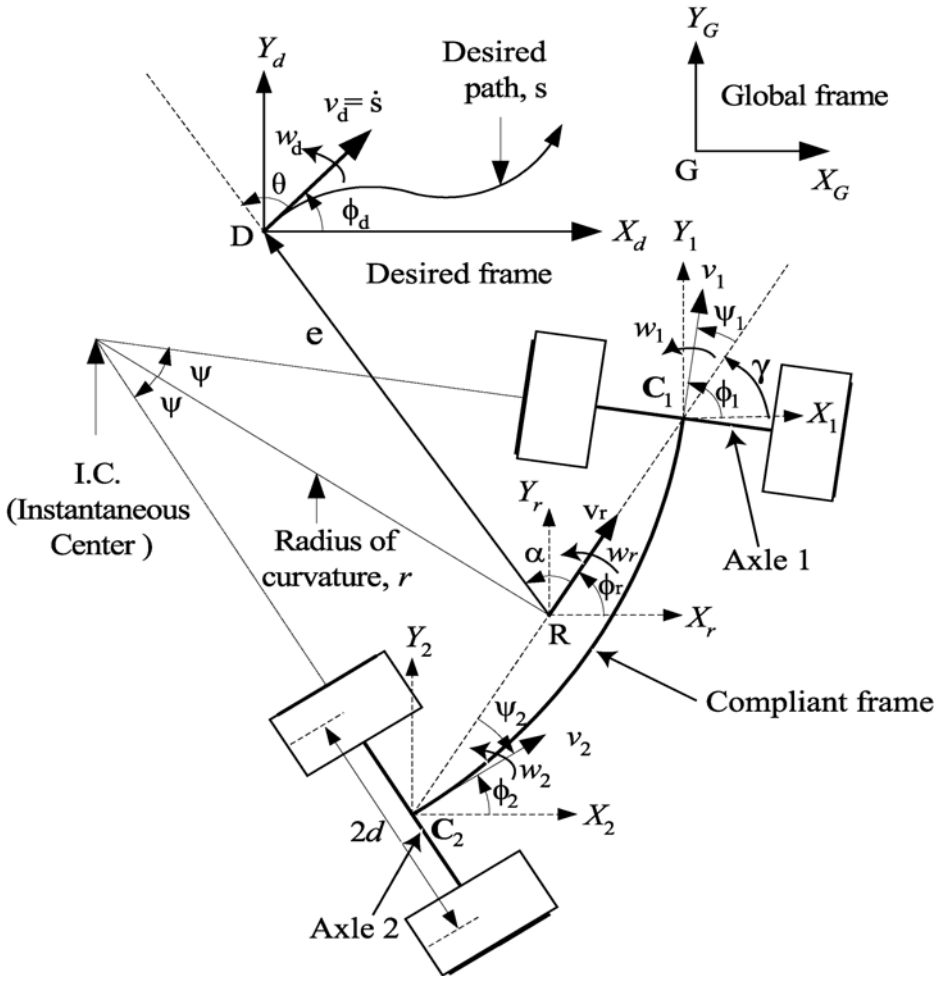

Figure 3.3. The two-axle CFMMR.

robot, Figure 3.4, let us define a fixed global reference frame $G(X,Y)$ and moving frames $f_i(x_i, y_i)$ attached to the points C_i at the midpoint of the i^{th} axle, where $i = 1,2$, Figure 3.3. At any instant, the i^{th} axle module is rotating about the IC (Instantaneous Center), such that the IC's projections onto the x_i axes define point C_i at the midpoint of each axle. A module configuration vector $q_i = [x_i \quad y_i \quad \phi_i]$ is then attached to this point for each axle. We then have the dynamic model:

$$\begin{aligned} &\mathbf{M}_i(q_i)\ddot{q}_i + \mathbf{V}_i(q_i, \dot{q}_i)\dot{q}_i + \mathbf{F}_i(\dot{q}_i) + \mathbf{G}_i(q_i) + \tau_{d,i} \\ &+\mathbf{F}_{K,i}(q_i, q_{i\pm1}) = \mathbf{E}_i(q_i)\tau_i - \mathbf{A}_i^T(q_i)\lambda_i \end{aligned} \tag{3.1}$$

where $\mathbf{M}_i(q_i) \in R^{3\times3}$ is a symmetric, positive definite inertia matrix for the i^{th} axle module. $\mathbf{V}_i(q_i, \dot{q}_i) \in R^{3\times3}$ is the centripetal and Coriolis forces, $\mathbf{F}_i(\dot{q}_i) \in R^{3\times1}$ denotes the friction, $\mathbf{G}_i(q_i) \in R^{3\times1}$ is the gravitational vector, $\tau_{d,i}$ denotes bounded unknown disturbances including unstructured unmodeled dynamics, $\mathbf{E}_i(q_i) \in R^{3\times2}$ is the input transformation matrix, $\tau_i \in R^{2\times1}$ is the input torques, and $\lambda_i \in R^{1\times1}$ is the vector of nonholonomic constraint

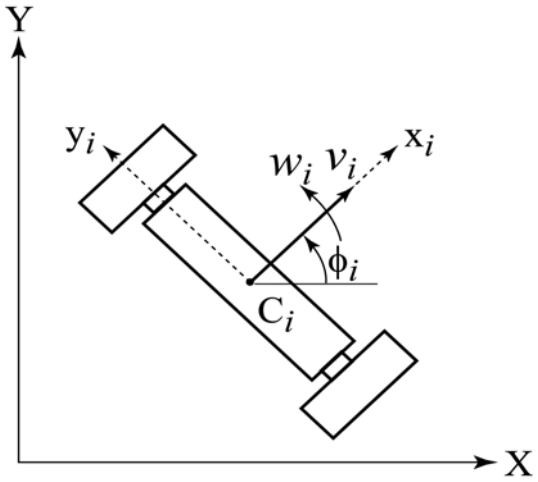

Figure 3.4. The i^{th} axle module.

forces. $\mathbf{A}_i(q_i) \in R^{1\times 3}$ is the global matrix associated with the nonholonomic constraints. $\mathbf{F}_{K,i}(q_i, q_{i\pm 1}) \in R^{3\times 1}$ represents the compliant frame forces, which impose additional physical constraints dependent upon flexible beam interaction.

Physical constraints, then, include nonholonomic constraints, $\mathbf{A}_i(q_i)\dot{q}_i = \mathbf{0}$, imposed by the wheels and curvature and velocity constraints imposed by the compliant frame [1]. The kinematic controller acts to coordinate axle commands such that all physical constraints are satisfied a priori. The axle level dynamic controller is then based upon Equation (3.1) in order to consider all forces acting upon the axle.

3.4 Motion Control and Sensing Strategy

Given the two-axle CFMMR, the control objective is to solve multiple navigation problems using a general approach. These include posture regulation, path following and trajectory tracking.

Let us analyze the target system first. Compared to the traditional unicycle-type wheeled mobile robot, the CFMMR also has physical constraints imposed by the frame in addition to nonholonomic constraints. The frame also complicates the dynamics by introducing highly nonlinear compliance. Resulting forces are quite dependent on the ability of the measurement system to predict relative axle posture, and thus the data fusion and instrumentation systems must be modified to improve relative position sensing.

According to the control objective and characteristics of the CFMMR, the motion control and sensing architecture is proposed, Figure 3.2. In order to characterize the performance of this architecture, the tracking errors due to the kinematic motion controller, dynamic motion controller, and sensing algorithms are defined as,

$$\begin{aligned} q_r - q_d &= e_k \\ q_s - q_r &= e_d \\ q - q_s &= e_s \end{aligned} \tag{3.2}$$

where q_d is the desired trajectory according to the virtual desired frame D, Figure 3.3, q_r is the reference trajectory created by the kinematic controller that the dynamic motion controller refers to, q_s is the trajectory estimates from the sensory system, and q is the actual trajectory of the axles. Components of q_d and q_r are shown in Figure 3.3. We then desire to minimize the total tracking error, e_{tot}, which is expressed as,

$$e_{tot} = q - q_d = e_k + e_d + e_s \,. \tag{3.3}$$

The norm of the total tracking error, $\|e_{tot}\|$, is then,

$$\|e_{tot}\| = \|e_k + e_d + e_s\| \le \|e_k\| + \|e_d\| + \|e_s\| \,. \tag{3.4}$$

Thus, to minimize the total tracking error, each component error should be minimized,

$$\min(\|e_k\| + \|e_d\| + \|e_s\|) = \min(\|e_k\|) + \min(\|e_d\|) + \min(\|e_s\|) \,. \tag{3.5}$$

In the following sections, the kinematic motion controller, dynamic motion controller, and sensory system are designed to minimize $\|e_k\|, \|e_d\|$ and $\|e_s\|$, respectively in lieu of physical constraints due to the cooperative configuration, i.e. the compliant frame on CFMMR.

3.5 Kinematic Motion Controller

According to the proposed control architecture, the kinematic motion controller considers physical constraints and provides the reference velocity inputs to the dynamic motion controllers. As shown in Figure 3.3, suppose that a desired trajectory, $q_d = [x_d, y_d, \phi_d]$, is produced by the desired linear and angular velocities, v_d and ω_d such that the path has curvature κ_d. The kinematic motion controller is designed such that,

1. The robot is asymptotically driven to the desired trajectory using the reference velocity inputs v_r and ω_r such that $\|e_k\| = 0$.

2. The path of the robot produced by the reference velocity inputs v_r and ω_r will not violate physical constraints at any point of the path. Then, the compliant frame curvature is limited to a certain value related to the physically feasible configurations. Since the compliant frame forces, $\mathbf{F}_{K,i}$, are a function of the two axle postures $(q_i, q_{i\pm1})$, they are bounded for all the robot configurations during the navigation given the kinematic motion controller.

3. The kinematic motion controller should be based on ideal kinematics, e.g., no feedback signal should be introduced from the actual robot since this perturbs convergence of the kinematic controller.

4. The compliant frame should be subjected to pure bending ($\psi = \psi_1 = -\psi_2$), Figure 3.3. This minimizes disturbance forces acting on the dynamic controller [1] and improves performance of the sensory system [18].

Polar coordinates (e, θ, α), Figure 3.3, are used to describe the reference configuration, q_r, and the reference velocity inputs are designed according to requirements <1> and <2> as,

$$\begin{aligned} v_r &= u_1(e,\theta,\alpha) \\ \omega_r &= u_2(e,\theta,\alpha) \end{aligned}. \tag{3.6}$$

The controlled system then becomes,

$$\begin{aligned} \dot{e} &= f_1(e,\theta,\alpha,v_r,\omega_r) = f_1'(e,\theta,\alpha) \\ \dot{\theta} &= f_2(e,\theta,\alpha,v_r,\omega_r) = f_2'(e,\theta,\alpha) \\ \dot{\alpha} &= f_3(e,\theta,\alpha,v_r,\omega_r) = f_3'(e,\theta,\alpha) \end{aligned} \tag{3.7}$$

where the polar configuration of the robot goes to the equilibrium point ($e = \theta = \alpha = 0$) as time goes to infinity, i.e., $\|e_k\| = 0$.

If the velocity inputs have small perturbations, $\hat{v}_r = v_r + \delta v_r$ and $\hat{\omega}_r = \omega_r + \delta\omega_r$ where $\delta v_r \neq 0$ and $\delta\omega_r \neq 0$, which happens if <3> is violated, then requirement <1> cannot be guaranteed. Under the perturbed velocity input the controlled system becomes

$$\begin{aligned} \dot{\tilde{e}} &= f_1'(\tilde{e},\tilde{\theta},\tilde{\alpha}) + g_1(\tilde{e},\tilde{\theta},\tilde{\alpha},\delta v_r,\delta\omega_r) \\ \dot{\tilde{\theta}} &= f_2'(\tilde{e},\tilde{\theta},\tilde{\alpha}) + g_2(\tilde{e},\tilde{\theta},\tilde{\alpha},\delta v_r,\delta\omega_r) \\ \dot{\tilde{\alpha}} &= f_3'(\tilde{e},\tilde{\theta},\tilde{\alpha}) + g_3(\tilde{e},\tilde{\theta},\tilde{\alpha},\delta v_r,\delta\omega_r) \end{aligned} \tag{3.8}$$

where

$$\begin{aligned} g_1(\tilde{e},\tilde{\theta},\tilde{\alpha},0,0) &= 0 \\ g_2(\tilde{e},\tilde{\theta},\tilde{\alpha},0,0) &= 0 \\ g_3(\tilde{e},\tilde{\theta},\tilde{\alpha},0,0) &= 0 \end{aligned}. \tag{3.9}$$

Then for $\delta v_r \neq 0$ and $\delta\omega_r \neq 0$, the new equilibrium point is nonzero, which violates requirement <1>. The requirement <3> is therefore proven.

In order to satisfy the above requirements, a centralized kinematic motion controller is presented as [17],

$$v_r = \frac{\left\{ \begin{array}{l} k_1 e\sqrt{\zeta - \cos 2\theta}\,\tanh(e - r\sqrt{2}\sqrt{\zeta - \cos 2\theta}) \\ +v_d e\cos\theta\sqrt{\zeta - \cos 2\theta} + v_d r\sqrt{2}\sin 2\theta\left(\sin\theta + \kappa_d e\right) \end{array} \right\}}{e\sqrt{\zeta - \cos 2\theta} + r\sqrt{2}\sin 2\theta\sin\alpha}$$
$$\omega_r = k_2\tanh(\theta + \alpha) + \frac{2}{e}\left(v_r\sin\alpha - v_d\sin\theta\right) - v_d\kappa_d \qquad (3.10)$$

where r is the radius of a circular *path manifold*. ζ=1+ε and ε is a sufficiently small perturbation. Refer to [17] for detailed derivation of this controller.

Since the above kinematic motion controller is centralized, the cascade connection was developed to provide commands to each axle [1]. To satisfy the pure bending requirement <4>, ψ may be solved numerically using the expression for the path radius of point *R*,

$$\frac{1}{r} = \frac{2\psi}{L\cos\psi}\ , \qquad (3.11)$$

where L is the frame length. Hence the linear and angular velocities of each axle, $v_{r,i}$ and $\omega_{r,i}$ are obtained by

$$v_{r,i} = \frac{v_r}{\cos\psi} + \frac{(-1)^i}{6}L\psi\dot{\psi} \qquad \left\{ \begin{array}{l} i = 1 \text{ for front axle} \\ i = 2 \text{ for rear axle} \end{array} \right.$$
$$\omega_{r,i} = \omega_r + (-1)^{i-1}\dot{\psi}\ . \qquad (3.12)$$

which satisfies physical constraints imposed by the frame.

In the centralized kinematic controller, the velocity (v_r, ω_r) of the middle point of the front and rear axle units, R, was introduced as the auxiliary centralized states, Figure 3.3. These centralized states were then passed between the axle units using the cascade connection mentioned above. The limitation of the centralized kinematic controller is that

scalability of the aforementioned controller to multiaxle configurations is not trivial, which is the subject of future work [19].

3.6 Dynamic Motion Controller

Using the proposed architecture, the dynamic motion controller provides wheel torque commands to the robot based upon the reference trajectory from the kinematic motion controller ($q_{r,i}, v_{r,i}, \omega_{r,i}$). The dynamic motion controller is designed such that,

1. Dynamic motion control is distributed for scalability and reduced axle level computational burden.

2. Model based frame interaction force estimates are included in the controller such that frame force disturbances on e_d are reduced.

3. Each axle follows the individual reference trajectories from the kinematic motion controller robustly using wheel torque commands. When the CFMMR works on rough terrain or even more complicated environments, the compliant frame forces might not be estimated accurately enough. So the dynamic motion controller should be robust and adaptive to the uncertainties caused by the complex interaction forces and the other dynamic disturbances. The trajectory tracking error should be uniformly bounded based on the bounded compliant frame forces, i.e., $\|e_d\| \le \varepsilon_d, \varepsilon_d > 0$.

In order to satisfy all the three requirements, a distributed motion controller is given by [2, 17]

$$\tau_i = -(\mathbf{S}_i^T \mathbf{E}_i)^{-1} K_i \mathbf{e}_{c,i} \|\xi_i\|^2 . \tag{3.13}$$

Here

$$\xi_i^T = \left\{ \|\mathbf{v}_i\| \|\mathbf{v}_i\|, \|\mathbf{v}_i\|, \|\mathbf{v}_{r,i}\|, \|\dot{\mathbf{v}}_{r,i}\|, 1, \|\mathbf{F}_{K,i}(q_{s,i}, q_{s,i\pm1})\| \right\} \tag{3.14}$$

$$\mathbf{e}_{c,i} = \mathbf{v}_i - \mathbf{v}_{c,i} \tag{3.15}$$

$$\mathbf{v}_{c,i} = \begin{bmatrix} v_{r,i} \cos e_{\phi,i} + k_{X,i} e_{X,i} \\ \omega_{r,i} + k_{Y,i} v_{r,i} e_{Y,i} + k_{\phi,i} v_{r,i} \sin e_{\phi,i} \end{bmatrix} \tag{3.16}$$

$$\begin{bmatrix} e_{X,i} & e_{Y,i} & e_{\phi,i} \end{bmatrix}^T = \mathbf{R}_{\phi,i} \left(q_{r,i} - q_{s,i} \right) \tag{3.17}$$

$$\mathbf{R}_{\phi,i} = \begin{bmatrix} \cos\phi_{s,i} & \sin\phi_{s,i} & 0 \\ -\sin\phi_{s,i} & \cos\phi_{s,i} & 0 \\ 0 & 0 & 1 \end{bmatrix} \tag{3.18}$$

$$\mathbf{E}_i = \frac{1}{r_w} \begin{bmatrix} \cos\phi_{s,i} & \sin\phi_{s,i} & -d \\ \cos\phi_{s,i} & \sin\phi_{s,i} & d \end{bmatrix}^T \tag{3.19}$$

$$\mathbf{S}_i^T = \begin{bmatrix} \cos\phi_{s,i} & \sin\phi_{s,i} & 0 \\ 0 & 0 & 1 \end{bmatrix} \tag{3.20}$$

where ξ_i is a known, positive definite vector. $K_i = \begin{bmatrix} K_{1,i} & 0 \\ 0 & K_{2,i} \end{bmatrix}$ is the matrix control gain and $K_{1,i}$, $K_{2,i}$ $k_{X,i}$, $k_{Y,i}$ and $k_{\phi,i}$ are positive constants. $\mathbf{v}_i = \begin{bmatrix} v_{s,i} & \omega_{s,i} \end{bmatrix}^T$ is the estimated axle velocity vector obtained from the sensory system. The r_w and d are wheel radius and half axle length respectively, Figure 3.3. $\mathbf{F}_{K,i}$ is the estimated frame force vector [2]. For the detailed derivation of these equations, refer to [2].

3.7 Sensory System

The sensor system provides posture and velocity feedback to the dynamic motion controllers according to the proposed architecture, Figure 3.5. The sensor system is designed such that,

1. Independent sensors are distributed on each axle.

2. Cooperative sensors provide relative posture estimates between neighboring axles.

3. Sensor data (either independent or cooperative) is fused to minimize posture estimate error, Figure 3.5, i.e., $\|e_s\| \le \varepsilon_s, \varepsilon_s > 0$.

4. Sensor fusion is distributed for scalability and reduced axle level computational burden.

Traditional independent sensors (odometry, inertial measurements, and even GPS) fused with common model based Extended Kalman Filters (EKF) provide axle posture estimates that are prone to drift and uncertainty. Such estimates are insufficient for managing cooperation amongst robots where interaction forces may occur. This is the case of the CFMMR, where frame compliance can cause large interaction forces due to drift in relative axle posture estimates. Thus, requirement <2> specifies that cooperative

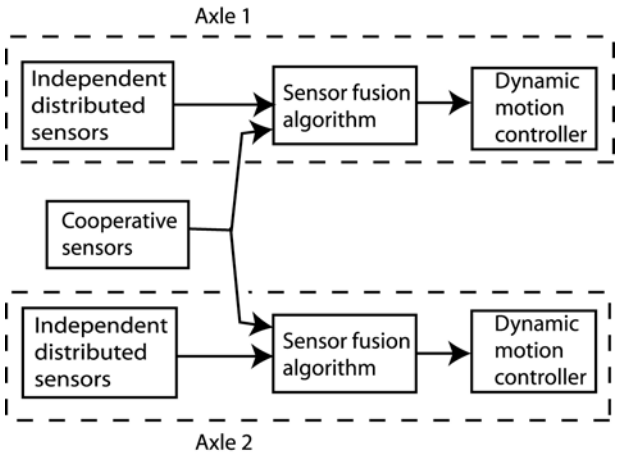

Figure 3.5. Sensor fusion algorithm block diagram

sensors be provided to bound relative posture estimate error.

A sensory system incorporating Relative Position Sensors (RPS) is presented to satisfy the above requirements [18, 20]. The cooperative RPS consists of a series of strain gauges placed at known locations along the length of the compliant frame in order to provide a strain polynomial. The relative posture (x_{RPS}, y_{RPS}, ϕ_{RPS}) of one axle to the other is calculated by piecewise integration of dx, dy and $d\phi$. Assuming sufficiently small step size, dL, the dx, dy and $d\phi$ can be calculated as:

$$\begin{aligned} d\phi &= dL / \rho \\ dx &= \rho \sin(d\phi) \\ dy &= \rho(1 - \cos(d\phi)) \end{aligned} \tag{3.21}$$

where the frame radius of curvature, ρ, is obtained directly from the strain polynomial.

The EKF is used as the first tier of the sensor fusion algorithm in order to provide axle level posture estimates based upon independent sensors. Since these estimates will drift and provide poor relative axle posture estimates, the Covariance Intersection (CI) filter is used for second tier data fusion to combine EKF and RPS data to bound relative posture estimates. Identical implementations of these fusion algorithms operate on each axle module.

3.8 Experimental Evaluations

3.8.1 Methods and Procedures

The distributed cooperative motion control architecture for the two-axle CFMMR was simulated in Matlab® and Simulink® to adjust control gains, but the results are not shown here. Experiments were conducted on a two-module CFMMR experimental

platform, Figure 3.1, at the University of Utah. The robot is controlled via tether by a dSpace™ 1103 DSP and power is supplied externally. Geared DC motors actuate each wheel and encoders provide position and velocity. Odometry and the relative position sensor are used in the sensing system. Two 7.2v RC car batteries are mounted on the rear axle to power the RPS amplifying circuit. The sampling frequency of the experiments was 100 Hz in order to arrive at a compromise between the computational limits of the DSP, velocity sensor noise attributed to higher sampling rates, and robust controller chatter at lower sampling rates.

The architecture is evaluated using the algorithms presented in Sections 3.5 to 3.7 while performing posture regulation. The evaluations were conducted on surfaces with increasing difficulty and realism: flat carpet (C), sand (S), and sand with scattered rocks (SR). Carpet provides high traction and emphasizes the capability of the kinematic and dynamic motion controllers under ideal circumstances. Sand provides lower traction and emphasizes the importance of the sensory system. Sand-and-rock introduces difficulty and demonstrates robustness to disturbances.

Nonideal algorithms were also evaluated to justify the proposed architecture. These include a nonideal kinematic motion controller [17], a traditional backstepping dynamic motion controller [21], and a traditional odometry based sensor system. Comparison experiments were operated on sand or carpet depending on whether controller or sensory system performance was being evaluated. The nonideal kinematic motion controller (FB) in [17] had the actual velocity fed into the kinematic controller, which does not satisfy <3> in Section 3.5. The dynamic motion controller (NR) in [21]

was not robust, which violates <3> in Section 3.6. The odometry sensor system (OD) did not have any cooperative sensors, which does not satisfy <2> in Section 3.7.

Overall, seven experimental tests are reported with each test consisting of five trials. The initial posture of the middle point R for each test is [x y ϕ] = [-1.342m -1.342m 0°]. At the end of each trial, the final robot posture is manually measured relative to a string-grid system suspended just above the robot to determine actual final position error, E, and off-tracking, $\Delta = \gamma - \phi$. Under ideal circumstances when pure bending is maintained, the orientation of the line $\overline{C_1C_2}$, represented by γ equals the actual heading angle, ϕ, of the velocity at point R, Figure 3.3. Off-tracking, Δ, indicates the ability of the dynamic controller and sensor system to maintain pure bending. Standard deviations, σ_E and σ_Δ, are reported for manual measurements to indicate consistency. For each test, we also report position error magnitude and orientation provided by the kinematic controller $\left[E_k, e_k^\phi\right]$, dynamic controller $\left[E_d, e_d^\phi\right]$, and sensory system $\left[E_s, e_s^\phi\right]$. A successful trial is defined only if the robot can complete the posture regulation task in this trial. The success rate is defined as the number of all successful trials over the total number of trials.

3.8.2 Experimental Results and Discussion

Table 3.1 shows the final posture errors for all the tests according to odometry and manual measurements. The proposed control architecture (Tests 1, 5, 7) performs as expected. In all of these tests, the kinematic controller produces zero position error, E_k, and zero orientation error, e_k^ϕ. Error produced by the dynamic motion controller (E_d, e_d^ϕ) and the sensor system (E_s, e_s^ϕ) both contribute to the actual error measured at the final posture. The system performance is relatively consistent with expectations. Relative to

Table 3.1. Experimental final posture error.

No	Surf	System kin +dyn +sens	Kinematic. Contr. Err.		Dyn. Contr. Err.		Sensor Error		Actual Error			
			E_k (cm)	e_k^ϕ (deg)	E_d (cm)	e_d^ϕ (deg)	E_s (cm)	e_s^ϕ (deg)	E $\pm\sigma_E$ (cm)	Δ $\pm\sigma_\Delta$ (deg)	Incr. err. (%)	Succ. Rate (%)
1	C	I+I+I	0	0	1.4	9.2	9.8	0.6	9.9 ±1.0	-2.0 ±3.5		100
2	C	FB+I+I	17.3	-2.0	4.6	27.9	4.0	-36.6	21.9 ±0.8	30.8 ±8.8	121	100
3	C	I+NR+I	0	0	34.5	12.0	24.8	-5.2	17.5	0.6	76	40
4	C	I+I+OD	0	0	4.4	6.6	9.2	7.1	10.6 ±3.4	-8.3 ±4.4	7	100
5	S	I+I+I	0	0	0.6	13.2	18.2	-15.6	17.9 ±1.6	0.9 ±2.0	80	100
6	S	I+I+OD	0	0	0.5	11.0	21.3	-8.0	21.6 ±8.5	-8.3 ±18.4	21(wrt No.5)	100
7	SR	I+I+I	0	0	0.8	15.8	18.0	-16.2	17.6 ±8.3	6.1 ±2.2	78	100

carpet (Test 1) E is increased by 80% on sand (Test 5) and 78% on sand-rock (Test 7). Increased disturbance is expected on these surfaces, although larger error is expected on sand-rock. Consistent with expectations, though, off-tracking is the least on sand. The sand allows the wheels to slip and reduce traction forces attributed to off-tracking. Overall, it can be observed from E_k, E_d, and E_s that the major source of error is produced by the sensing system, while a small amount of error results from the dynamic controller.

The nonideal kinematic motion controller with velocity feedback was used in Test 2. Compared to Test 1, E is increased by 121% and off-tracking, Δ, is increased by 1440% in Test 2. Velocity feedback also perturbed the kinematic motion controller and increased kinematic controller error (E_k, e_k^ϕ) significantly. Since the kinematic controller provides the reference trajectories to the dynamic controller, the dynamic control errors also became larger (E_d, e_d^ϕ). The posture errors were therefore increased significantly.

The nonrobust dynamic motion controller used in Test 3 also increased error and most of the trials failed. Position error, E, is 76% larger than Test 1. More importantly though, 60% of the trials failed to complete because the wheels collided during the maneuver due to off-tracking caused by nonrobustness of the controller. In the trials that did complete, the off-tracking is actually quite small, but this is NOT representative of this controller's performance. It is thus concluded that the system performance with nonrobust control is unreliable.

The sensor system is evaluated with just odometry feedback in Tests 4 and 6 on carpet and sand, respectively. Given the high traction provided by the carpet (Test 1), error E is only increased by 7% while off-tracking, Δ, is increased by 315%. This large increase in Δ illustrates the importance of the cooperative sensor. The sand surface (Test 6) underscores the importance of the cooperative sensing. Compared to Test 5, E is increased by 21% and Δ is increased by 822%, both with significantly increased standard deviations.

Figure 3.6 shows the robot using the proposed architecture during posture regulation on carpet (Test 1) and sand with rock (Test 7). The white lines represent the string grids and the black lines represent sensor system data. The solid black line represents the predicted position of the middle point R and the dashed black lines represent estimated positions of the wheels. The system performs nearly as well with sand-rock as it did with the ideal high traction carpet surface. This is a significant improvement over previous results without the proposed architecture where error on sand with rock was as large as 66 cm [1]. Overall, all of these results demonstrate the property

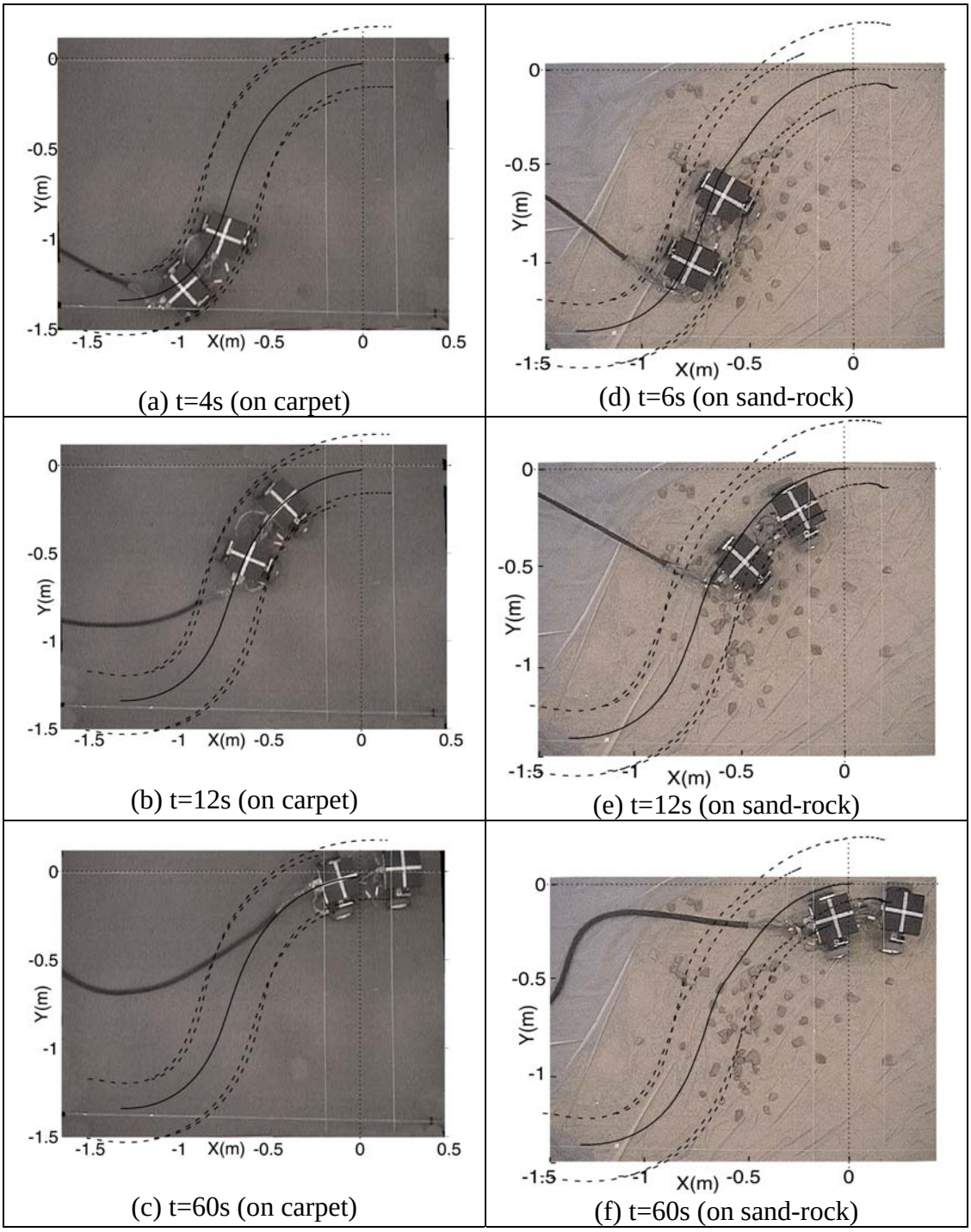

(a) t=4s (on carpet)

(d) t=6s (on sand-rock)

(b) t=12s (on carpet)

(e) t=12s (on sand-rock)

(c) t=60s (on carpet)

(f) t=60s (on sand-rock)

Figure 3.6. Robot paths during posture regulation on carpet and on sand-and-rock.

of the proposed distributed cooperative motion control and sensing system has superiority to robustly maneuver nonideal terrain with significant disturbances.

The proposed architecture will be extended to multiaxle configurations (more than two axles) in future work. The architecture itself is quite generic and simply establishes the interaction amongst kinematic controllers, dynamic controllers, and sensory system components. Customization and extension of the algorithms within these components is currently being examined for this purpose.

3.9 Conclusions

This paper proposes a distributed cooperative motion control and sensing architecture combining a kinematic motion controller, a dynamic motion controller, and a sensor fusion system incorporating a Relative Position Sensor for a two-axle compliant framed wheeled modular mobile robot. Experimental results demonstrate the efficiency and robustness of the proposed technique. This motion control and sensing strategy is generally applicable to other cooperative mobile robots. Future work will focus on extending these results to other CFMMR configurations and improving performance of the sensing system and dynamic controller.

CHAPTER 4

TERRAIN FEATURE LOCALIZATION

4.1 Introduction

The conclusions of Chapter 3 indicate that the position estimate error is the major source of tracking error for the CFMMR, especially operating on rough terrain. In many outdoor environments, traditional sensors are used to achieve localization, such as laser range sensors, vision sensors and sonar. But they need to detect physical landmarks to facilitate their localization, which does not work well for some outdoor situations. GPS is another popular tool for localization, but accuracy is limited and many environments block signals and preclude its application. Therefore, the goal of this research is to improve localization accuracy when the above traditional sensors are not suitable to use.

In this chapter, a novel terrain feature based localization technique is developed for mobile robots operating on uneven terrain. The hypothesis is the robots can localize themselves relative to a terrain map as they travel over the uneven terrain. Here the terrain map is defined to include terrain characteristic, such as terrain inclination, surface roughness, traction capability, etc. A topographical map can be used to extract the terrain map. While it is believed both terrain inclination and surface roughness can be used for identifying the position of the robot, only terrain inclination information is extracted and applied here to prove the hypothesis. This new method is similar to how a human hiker or

driver would localize themselves along a trail by recognizing the terrain characteristic of particular trail segments. Using this technique, localization can physically be performed with limited on-board sensors, such as tilt sensors and odometry. Thus the terrain characteristic is measured and the measurement data is used to fuse with the terrain map extracted from a known topographical map.

It is assumed that a specific path, such as a topographical map with a series of way points (x_d) is chosen according to the operator's judgment, and that obstacles and borders are identified in the map, Figure 4.1. Then a cross-section map is obtained along a vertical plane crossing the chosen path (x_d), Figure 4.2. Based on this cross-section map, a terrain inclination or slope map is extracted along that path (x_d), Figure 4.3. Unlike traditional techniques where physical landmarks define features in the map, the terrain inclination is treated directly as the feature of the environment for outdoor mobile robots in this research. A tilt sensor is used here to measure the terrain inclination. A standard

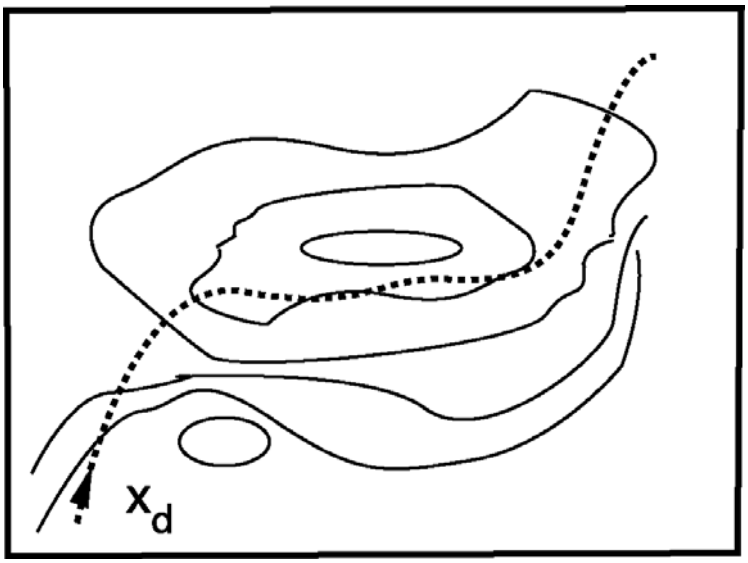

Figure 4.1. Overall topographical map.

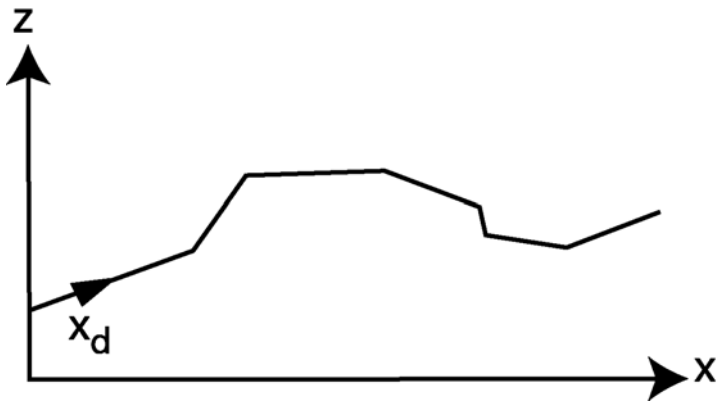

Figure 4.2. Cross section of elevation along the specified path with respect to the x-axis.

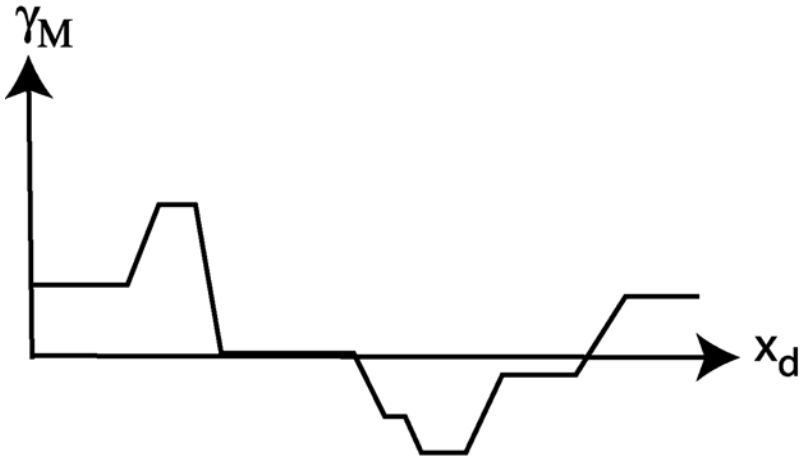

Figure 4.3. Inclination along the specified path.

Extended Kalman Filter (EKF) algorithm is used to incorporate the tilt sensor data over time to determine the position of the robot given the extracted terrain map, Figure 4.3.

The main contribution of this research involves a terrain feature based localization technique to allow the robot to identify its position relative to a terrain characteristic map. A terrain map extraction algorithm is derived, and an EKF algorithm is applied to achieve localization based on the extracted terrain map. Simulations then verify the terrain feature localization and demonstrate its capability to achieve localization on uneven terrain. This

terrain feature localization technique is generally applicable to other two-axle mobile robots even though the intended platform is the CFMMR.

The structure of this chapter follows. Background on the current literature is discussed in Section 4.2. The EKF terrain feature based localization technique is proposed in Section 4.3. Simulation results and discussion are presented in Section 4.4. Conclusions are described in Section 4.5.

4.2 Background

Mobile robots have been increasingly used in applications such as space exploration [22] and search and rescue [23] where the robots are required to travel over uneven terrain. In recent years, many aspects of research on mobile robots operating in rough terrain have been studied, such as rough terrain modeling [24, 25], terrain characterization [26, 27], and motion planning and control [25]. However, the effectiveness of motion control partly depends on the accuracy of mobile robot localization. Very few researchers have been found so far to focus on localization for rough terrain motion control [28] [29]. In the case of [28] [29], a 3-D laser range scanner was combined with a 2-D simultaneous localization and mapping algorithm for autonomous navigation in uneven environment. However, the laser scanners require a reliable determination of the landmarks and the ground, which is not practical for many outdoor situations.

In the last decades, significant investigation of mobile robot localization has been performed [30] [31]. According to the survey in [31], the traditional work on localization requires laser range finders [28, 29, 32], vision systems [33-35], and sonar [36, 37]. These sensors are used to measure the relative distance between the robots and some

static or dynamic landmarks or features. The assumption for this previous research was that landmarks could be found for localization. In many outdoor environments, however, the landmarks are not always identifiable, and may be unavailable for some environments. GPS is a popular solution to solve such outdoor localization problems [38, 39]. However, GPS is capable of at best decimeter accuracy and GPS signals might be unavailable in some cases. It is worth to note that terrain features have been used to achieve terrain following for military aircraft [40, 41], and bottom mapping/map matching [42] for underwater vehicles when GPS signals are lost. In these applications, terrain elevation maps are usually combined with elevation measurements to deduce the position of aircrafts or submarines so they can perform terrain contour following.

Inspired by terrain following and bottom mapping/map matching, this research brings a new localization method where the characteristics of the terrain, such as terrain inclination and terrain surface condition, are considered as features of the surroundings. Thus, this method can be applied to derive more exact localization relative to terrain features that the robot must navigate, and provides localization when other traditional landmarks are unavailable. This method can eventually be combined with other traditional techniques to improve the accuracy of the robot localization in general outdoor environments.

4.3 EKF Terrain Feature Based Localization

4.3.1 Terrain Map Extraction

Two-axle mobile robot is simplified as a line connecting the two wheel contact points C_1 and C_2, Figure 4.4. The assumption is made that only the slopes at C_2 can be

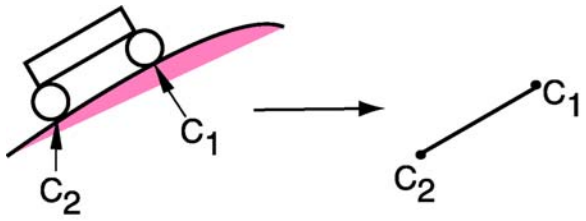

Figure 4.4. Simplified robot-terrain interaction diagram.

measured. Given a path, x_d, on a topographical map, a simple example of a cross-section of the topographical map $\{z \mid z = f_M(x)\}$ is shown in Figure 4.5. Then a terrain inclination map $\{\gamma_M \mid \gamma_M = h_M(x_d)\}$ needs to be extracted as a reference for slope measurement at the point C_2. The variable x_d represents the location of the robot on the path.

In this example, the whole map is divided into eight sections. The slope function is $h_M(x_d) = \gamma_{M0} = 0$ at $b_0 \le x \le b_1 - L$ or $d_0 = b_0 \le x_d \le b_1 - L = d_1$ where γ_{M0} is the slope of the first surface, S0. For $b_1 - L < x < b_1$ or $d_1 = b_1 - L < x_d < b_1 = d_2$, the front axle ($C_1$) moves to the surface S1 while the rear axle (C_2) is still on the surface S0. Therefore the slope at C_2 is between the γ_{M0} and γ_{M1} during this period. According to the geometric relationship in Figure 4.6 (a), the slope function is derived as,

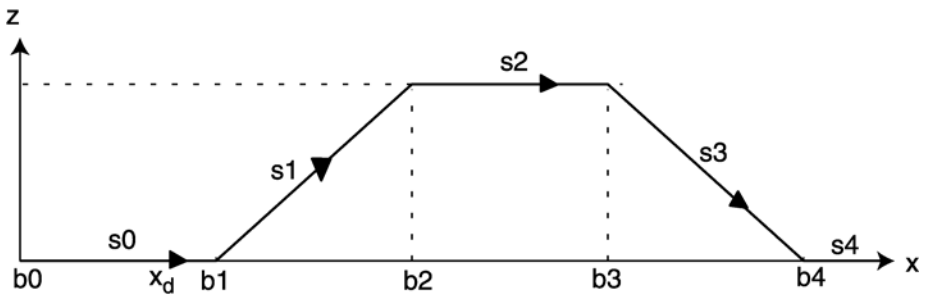

Figure 4.5. Elevation map.

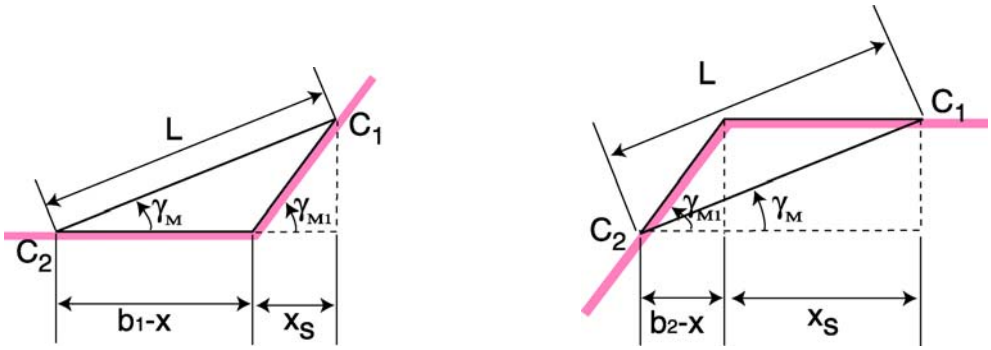

Figure 4.6. Geometric diagram.

$$h_M(x_d) = \sin^{-1}\left(\frac{x_s \tan\gamma_{M1}}{L}\right) \tag{4.1}$$

where x_s can be solved from $(1+\tan^2(\gamma_{M1}))x_s^2 + 2(b_1 - x_d)x_s + (b_1 - x_d)^2 - L^2 = 0$.

Then when C_2 moves on the surface S2, the slope function is $h_M(x_d) = \gamma_{M1}$ at $b_1 \le x \le b_2 - L$ or equivalently $d_2 = b_1 \le x_d \le \frac{b_2 - b_1}{\cos(\gamma_{M1})} + b_1 - L = d_3$. The slope function for $b_2 - L < x < b_2$ or $d_3 = \frac{b_2 - b_1}{\cos(\gamma_{M1})} + b_1 - L < x_d < \frac{b_2 - b_1}{\cos(\gamma_{M1})} + b_1 = d_4$ is obtained from the geometric diagram, Figure 4.6 (b), as,

$$h_M(x_d) = \sin^{-1}\frac{(b_2 - x)\tan(\gamma_{M1})}{L} = \sin^{-1}\frac{(\frac{b_2 - b_1}{\cos(\gamma_{M1})} - x_d + b_1)\sin(\gamma_{M1})}{L}. \tag{4.2}$$

Likewise, for the following sections, the slope functions are extracted as,

$$\{h_M(x_d) = \gamma_{M2} = 0 \,|\, \underbrace{\frac{b_2 - b_1}{\cos(\gamma_{M1})} + b_1}_{d_4} \le x_d \le \underbrace{b_3\text{-}b_2 + \frac{b_2 - b_1}{\cos(\gamma_{M1})} + b_1 - L}_{d_5}\}, \tag{4.3}$$

$$\{h_M(x_d) = -\sin^{-1}\frac{x_s \tan|\gamma_{M3}|}{L} \Big| \underbrace{b_3\text{-}b_2+\frac{b_2-b_1}{\cos(\gamma_{M1})}+b_1-L}_{d_5} < x_d < \underbrace{b_3\text{-}b_2+\frac{b_2-b_1}{\cos(\gamma_{M1})}+b_1\}}_{d_6} \tag{4.4}$$

where x_s can be solved from $(b_3-b_2-x_d+b_1+\frac{b_2-b_1}{\cos(\gamma_{M1})}+x_s)^2+\tan^2(\gamma_{M3})x_s^2-L^2=0$.

$$\{h_M(x_d) = \gamma_{M3} \Big| \underbrace{b_3\text{-}b_2+\frac{b_2-b_1}{\cos(\gamma_{M1})}+b_1}_{d_6} \le x_d \le \underbrace{\frac{b_4-b_3}{\cos|\gamma_{M3}|}+b_3\text{-}b_2+\frac{b_2-b_1}{\cos(\gamma_{M1})}+b_1-L\}}_{d_7}, \tag{4.5}$$

$$\{h_M(x_d) = -\sin^{-1}\frac{(\frac{b_4-b_3}{\cos|\gamma_{M3}|}-x_d+b_1+\frac{b_2-b_1}{\cos(\gamma_{M1})}+b_3-b_2)\sin|\gamma_{M3}|}{L} \Big| \underbrace{\frac{b_4-b_3}{\cos|\gamma_{M3}|}+b_3\text{-}b_2+\frac{b_2-b_1}{\cos(\gamma_{M1})}+b_1-L}_{d_7} < x_d < \underbrace{\frac{b_4-b_3}{\cos|\gamma_{M3}|}+b_3\text{-}b_2+\frac{b_2-b_1}{\cos(\gamma_{M1})}+b_1\}}_{d_8}, \tag{4.6}$$

$$\{h_M(x_d) = \gamma_{M4} = 0 \Big| x_d \ge \underbrace{\frac{b_4-b_3}{\cos|\gamma_{M3}|}+b_3\text{-}b_2+\frac{b_2-b_1}{\cos(\gamma_{M1})}+b_1\}}_{d_8}. \tag{4.7}$$

Therefore, the terrain inclination map is extracted as Figure 4.7 considering the simplified robot geometry. Then a polynomial fitted function of this terrain inclination map is generated for the following section.

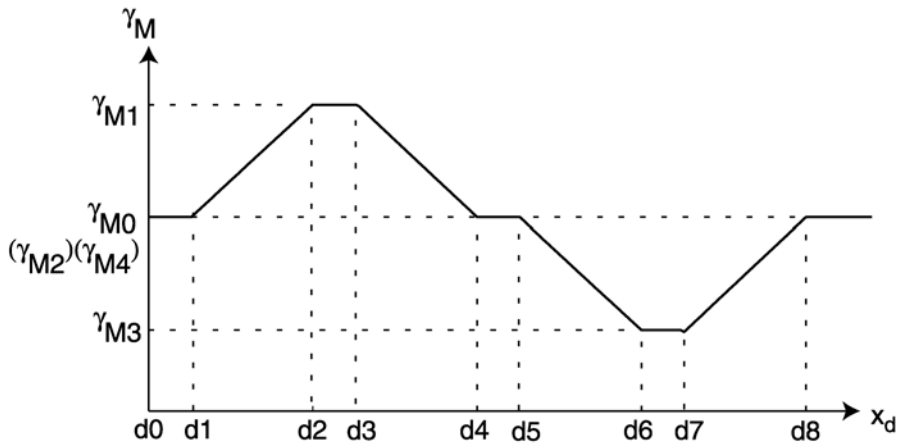

Figure 4.7. Terrain inclination map considering the robot geometry.

4.3.2 Extended Kalman Filter Terrain Feature Localization

The extended Kalman filter (EKF) is an extension of the Kalman filter for a nonlinear system. It consists of state transition probability and the measurement probability. The EKF is popular in mobile robotic application since most mobile robotic systems are nonlinear. An EKF localization algorithm is used here to determine the position of the robot relative to an extracted map $\{\gamma_M \,|\, \gamma_M = h_M(x_d)\}$ through slope sensing and motion. In this case, we assume that the initial position has an appreciable error, and that the probabilistic paradigms of the system state (x_d) and slope measurement (γ_T) can be represented by Gaussian distributions.

Following the notations in [30], the general form of the EKF is shown as,

$$X_t = g(u_t, X_{t-1}) + N(0, R_t) \tag{4.8}$$

$$Z_t = h(X_t, m) + N(0, Q_t) \tag{4.9}$$

where X_i is the system state, Z_i is the measurement and u_i is the control input at the i^{th} time interval. R_i and Q_i are the covariance matrices associated with the uncertainties of states and measurement, respectively. Given an appropriate motion and measurement model, the EKF localization algorithm requires as its input a Gaussian estimate of the robot position at time interval *t*-1, with mean μ_{t-1} and covariance $\sum_{t-1}$. It also requires a control input u_t, and a map *m*. Then the output of the EKF localization algorithm is a new, revised estimate μ_t and $\sum_t$.

Assume that the robot follows a known path with nonzero inclinations and that the robot can measure its inclination. The motion model is expressed as,

$$\begin{aligned} X_t &= x_{d,t} = x_{d,t-1} + \hat{v}_t T \\ &= x_{d,t-1} + v_t T + N(0, R_t) \end{aligned} \tag{4.10}$$

where $\hat{v}_t$ is the actual velocity, v_t is the control input u_t, and T is the sampling period. Then we have the nominal function of the system model as,

$$g(u_t, X_{t-1}) = x_{d,t-1} + v_t T \,. \tag{4.11}$$

The measurement model is obtained from the above extracted terrain map as,

$$\gamma_{T,t} = h_M(x_{d,t}) + N(0, Q_t) \tag{4.12}$$

where h_M is the polyfitted function of the terrain slope map extracted in the last section. The variation Q_t represents the slope measurement uncertainty and map inaccuracy.

Then the mean, $\bar{\mu}_t$, and covariance, $\bar{\Sigma}_t$, of the system state estimate, X_{t-1}, at the time interval t can be predicted from the state estimate at the previous time interval $t-1$ as,

$$\bar{\mu}_t = \mu_{t-1} + v_t T \tag{4.13}$$

$$\bar{\Sigma}_t = G_t \Sigma_{t-1} G_t^T + V_t M_t V_t^T \tag{4.14}$$

In the above equation, G_t is the Jacobian matrix with respect to the state, X_{t-1}, as,

$$G_t = \frac{\partial g(u_t, \mu_{t-1})}{\partial X_{t-1}} = v_t T \,. \tag{4.15}$$

The actual velocity is assumed to be composed of the nominal velocity plus Gaussian noise with zero mean value and the standard deviation $\alpha|v|$ where the coefficient α is dependent on the specific robot configuration. Hence the covariance matrix associated with the control input, M_t, is expressed as,

$$M_t = (\alpha|v_t|)^2 \,. \tag{4.16}$$

V_t is the Jacobian matrix with respect to the control input as,

$$V_t = \frac{\partial g(u_t, \mu_{t-1})}{\partial u_t} = T \,. \tag{4.17}$$

The next step is to correct the position of the robot according to the measurement and map. The new revised mean estimate, μ_t, and covariance estimate, $\sum_t$, are derived as,

$$\mu_t = \bar{\mu}_t + \bar{\Sigma}_t H_t^T (H_t \bar{\Sigma}_t H_t^T + Q_t)^{-1} (\gamma_{T,t} - h_M(\bar{\mu}_t)) \tag{4.18}$$

$$\Sigma_t = (I - \bar{\Sigma}_t H_t^T (H_t \bar{\Sigma}_t H_t^T + Q_t)^{-1} H_t) \bar{\Sigma}_t \tag{4.19}$$

where $\gamma_{T,t}$ is the slope measurement at the time interval *t*. H_t is the Jacobian matrix with respect to the states as,

$$H_t = \frac{\partial h(\bar{\mu}_t, m)}{\partial X_t} = h_M^{'}(\bar{\mu}_t) . \tag{4.20}$$

Therefore, given the estimated mean and uncertainty of the initial position, μ_0 and Σ_0, the robot position can be predicted using Equations (4.13) and (4.14) according to the system model, and then be updated using Equations (4.18) and (4.19) based on the measurement model.

4.4 Simulations

4.4.1 Methods and Procedure

The proposed EKF terrain localization algorithm was simulated in Matlab® and Simulink®. In the simulation, a cross section of a topographical map along a robot motion path is given, Figure 4.8, such that a terrain slope map can be extracted beforehand. Measurement noise was introduced to simulate the real tilt sensor signals.

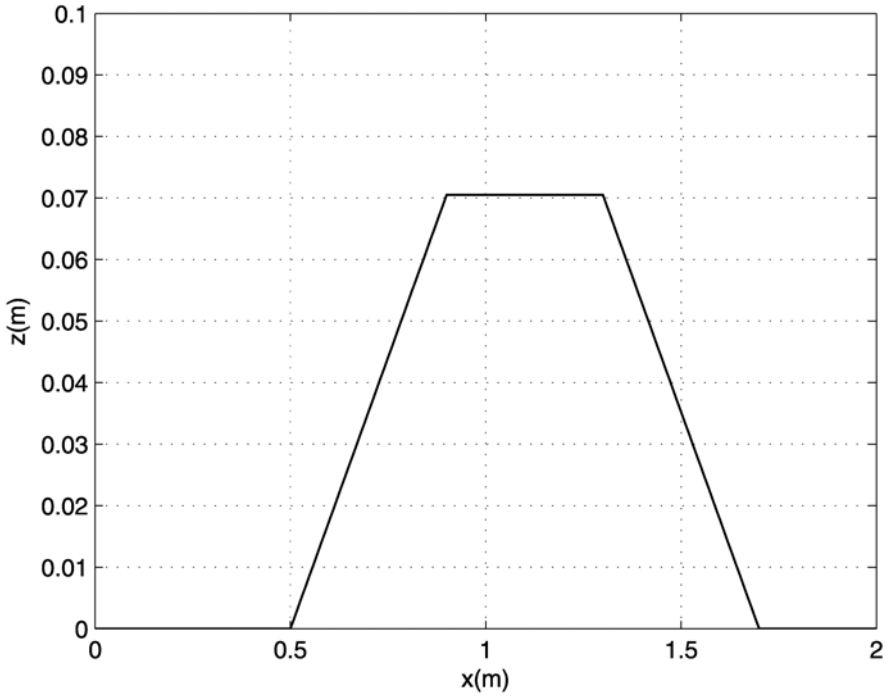

Figure 4.8. The simulated cross-section of a topographical map.

The measured slope data are then simulated as Figure 4.9. Given a typical reference velocity of $v = 0.2\ m/s$, the actual velocity, $\hat{v}$, is simulated as Figure 4.10 to incorporate the white noise on the reference velocity. According to the signal noise estimates, choose the velocity variation coefficient of $\alpha = 0.01$, and the measurement variation of $Q = 0.1$.

Three group settings are simulated to validate the proposed technique. In Case 1 and 2, a typical sampling period $T = 0.001\ s$ is applied. In Case 1, the mean and variation of the initial estimate $\mu_0 = 0.02\ m$, $\sigma_0 = 0.01$ are used to represent the initial error based on the assumption of an approximately known initial conditions in the last section. For Case 2, the mean and variation of the initial estimate is increased to $\mu_0 = 0.05\ m$, $\sigma_0 = 0.1$ to test how the algorithm responses to the larger initial errors. In Case 3, the initial conditions are the same as the Case 2, but the sampling period is increased to 0.01*s*

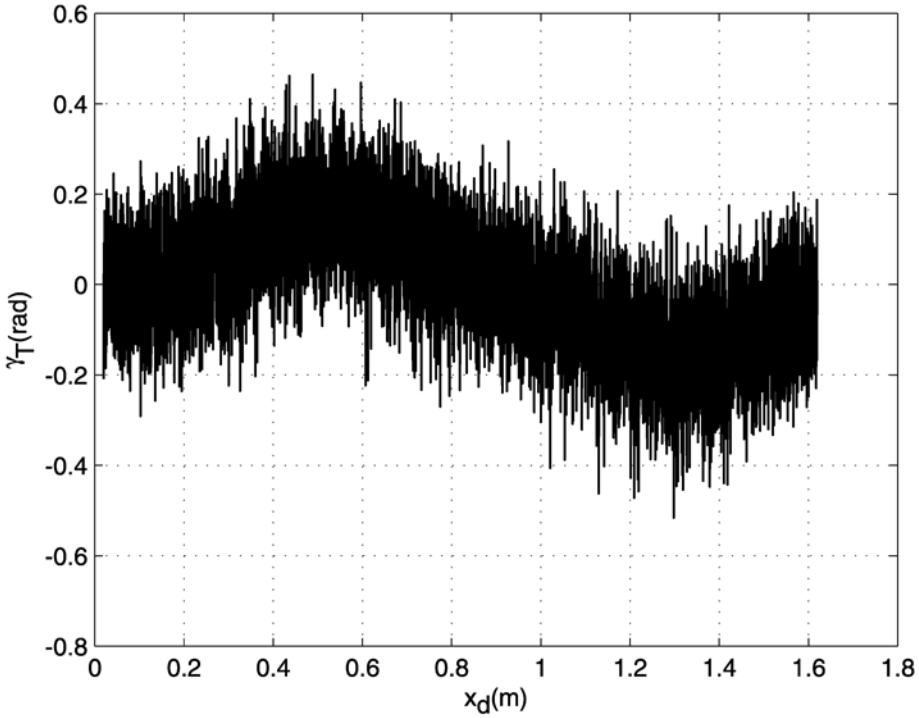

Figure 4.9. The measured slope data.

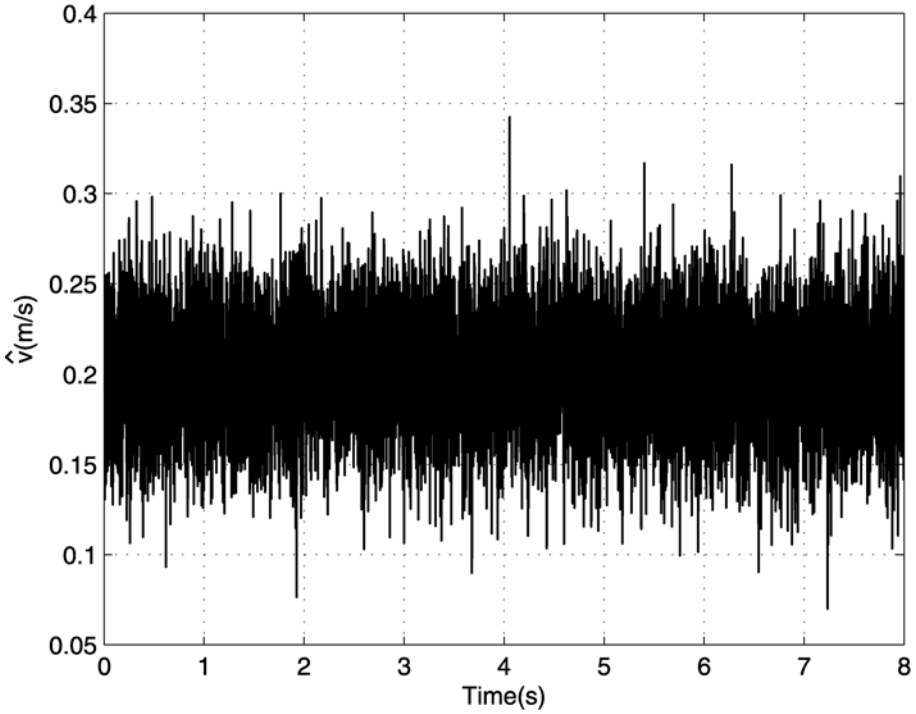

Figure 4.10. The actual linear velocity.

to test how the proposed algorithm will be affected by the different sampling periods.

4.4.2 Results and Discussion

Using the terrain map extraction algorithms in Section 4.3.1, the terrain inclination map is extracted from Figure 4.8, and fitted with a seventh order polynomial function to generate the EKF measurement model, Figure 4.11. However, as Figure 4.11 shows, the polyfitted function produces deviation from the extracted map.

Simulation results are shown in Figure 4.12 and Figure 4.13 for Case 1 when the initial position estimate is represented by $\mu_0 = 0.02$ m and $\sigma_0 = 0.01$. According to Figure 4.12, the mean position error settles down to –0.005 m in 2.3 seconds, jumps to 0.015 m at 4 seconds, and eventually settles down within ±0.005 m. Figure 4.13 shows the variation of the position error converges to zero in 2 seconds. When the initial estimates are changed to $\mu_0 = 0.05\ m$ and $\sigma_0 = 0.1$ in Case 2, the approximation of the initial position is less reliable compared with Case 1. According to Figure 4.14, the mean position error has much higher overshoot at the beginning of the simulation, and then settles down to the same range as Case 1. However, it still increases at about 4 seconds. The variation of the position error still converges well to zero even though the initial error is relatively large, Figure 4.15. As the sampling time is increased to 0.01 in Case 3, the simulation results, Figure 4.16, predict that the settling time becomes longer and the steady state error keeps within ±0.01 m which is much larger than Case 2. Also, the convergence of the variation becomes slower, Figure 4.17.

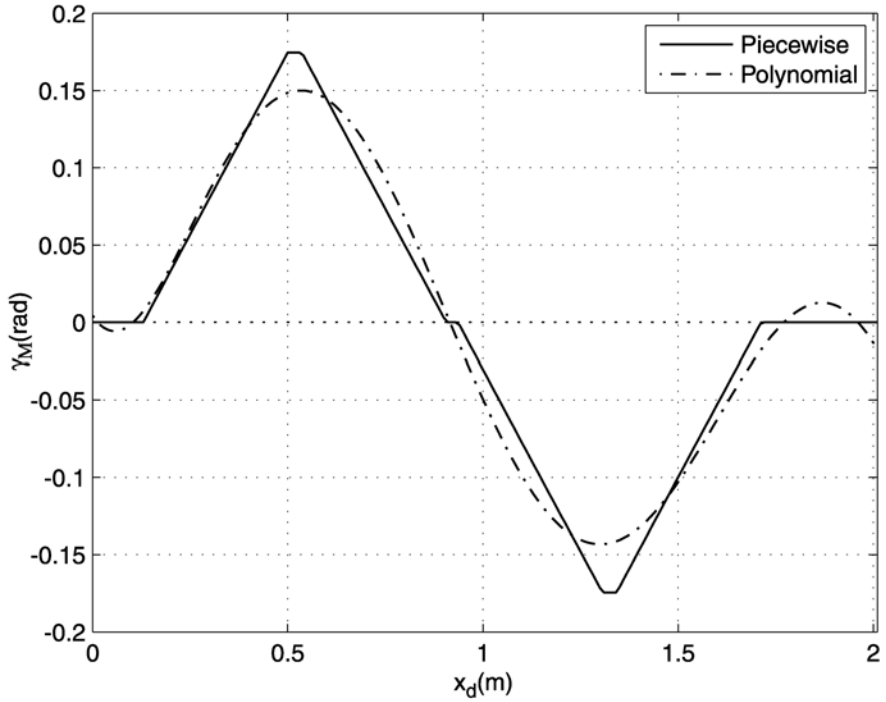

Figure 4.11. The terrain inclination map and its polynomial fitted function

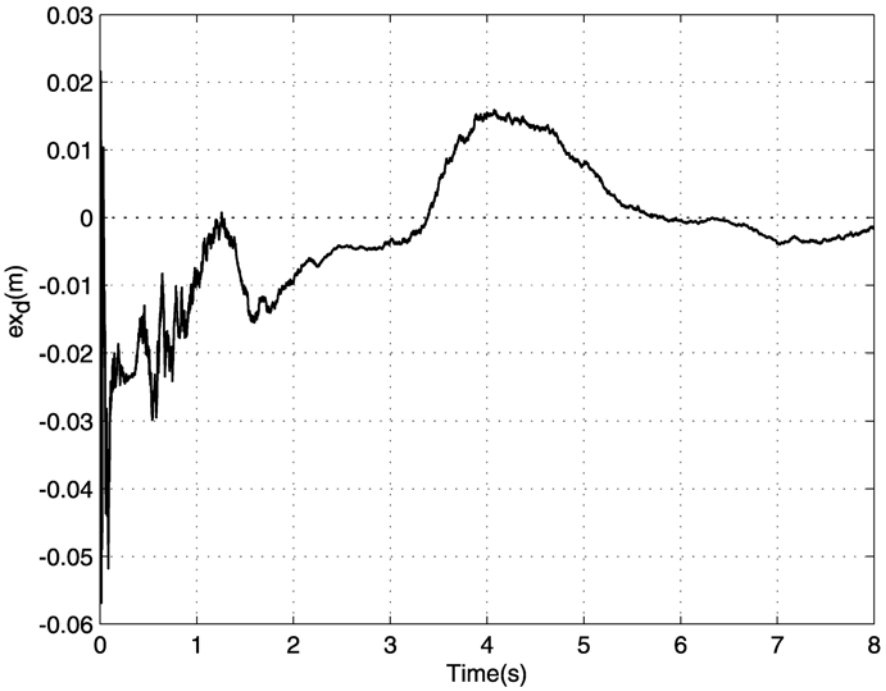

Figure 4.12. The mean position error for Case 1 where $\mu_0 = 0.02$ m and $\sigma_0 = 0.01$.

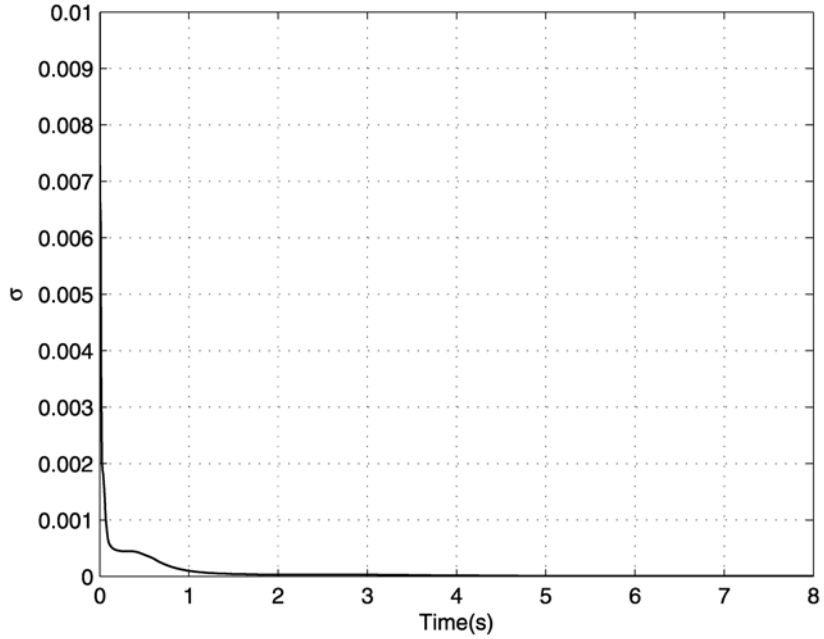

Figure 4.13. The variation of the position error for Case 1.

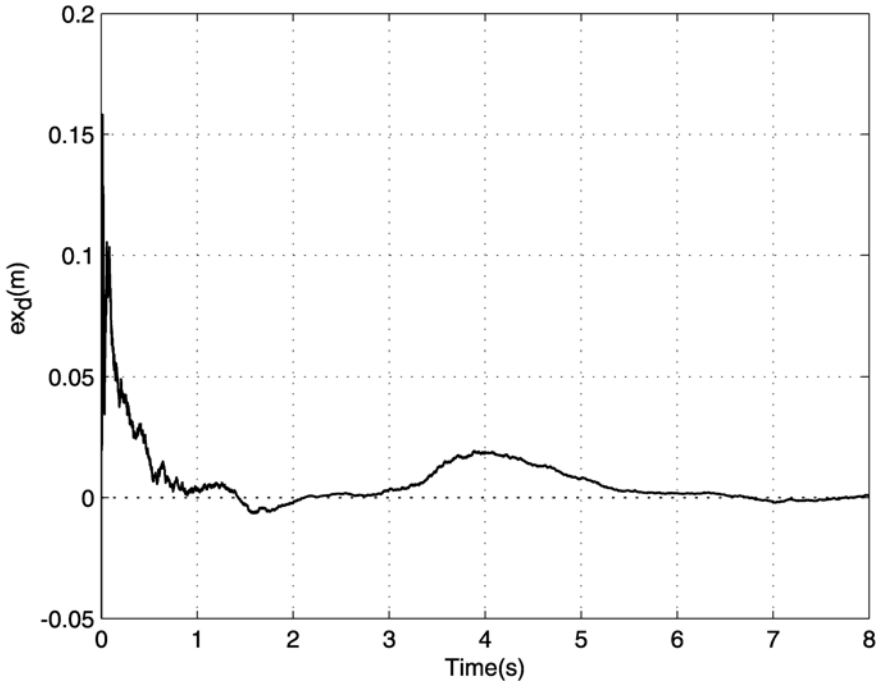

Figure 4.14. The mean position error for Case 2 where $\mu_0 = 0.05$ m and $\sigma_0 = 0.1$.

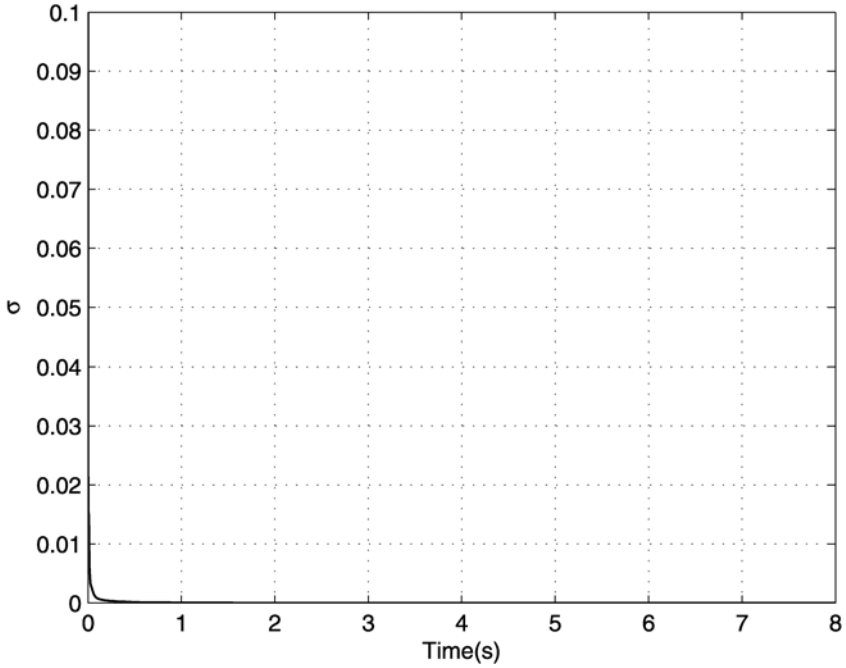

Figure 4.15. The variation of the position error for Case 2.

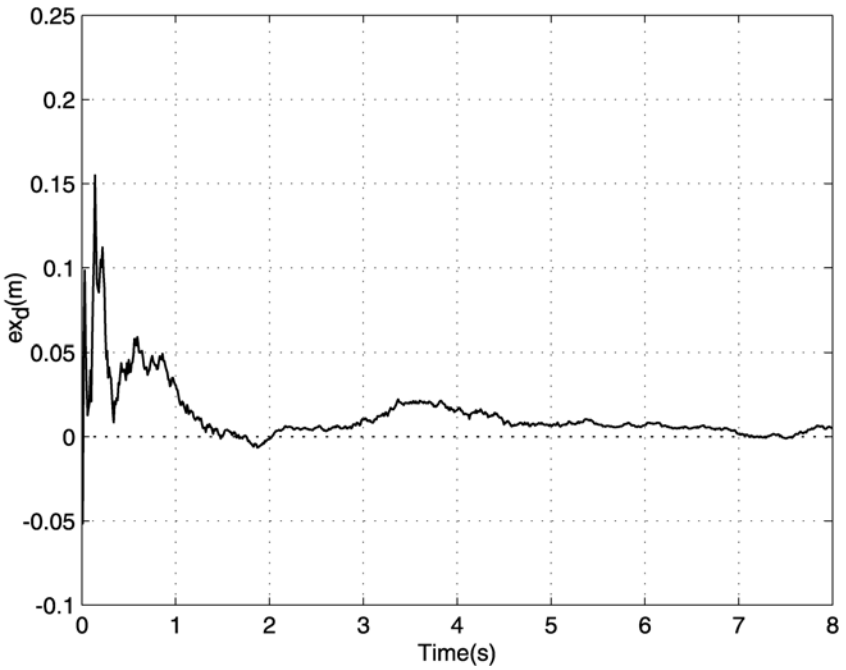

Figure 4.16. The mean position error for Case 3.

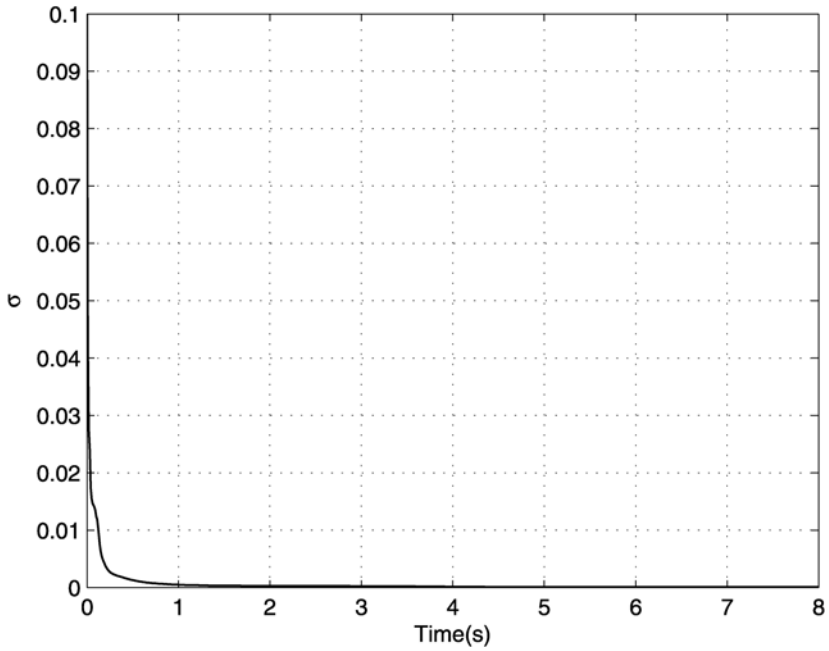

Figure 4.17. The variation of the position error for Case 3.

In order to analyze the source of the position errors, a polynomial function map is assumed and simulated. Simulation results indicate that the position error is much reduced, Figure 4.18, although small jumps still exist. Compared with Figure 4.12, it is believed that most of the position errors are caused by the deviation between the polyfitted function and the extracted map, and those small jumps are caused by the system noise. Hence, it is concluded that the proposed technique has capability to reject system bias but more sensitive to the sampling rate.

4.4.3 Future Work

The proposed terrain feature technique is demonstrated working on short trails. However, longer trails introduce additional challenges. The first issue is increased computation load for longer trails if a long polynomial map needs to be extracted. In order to reduce the computation, a long trail could be divided into a series of short

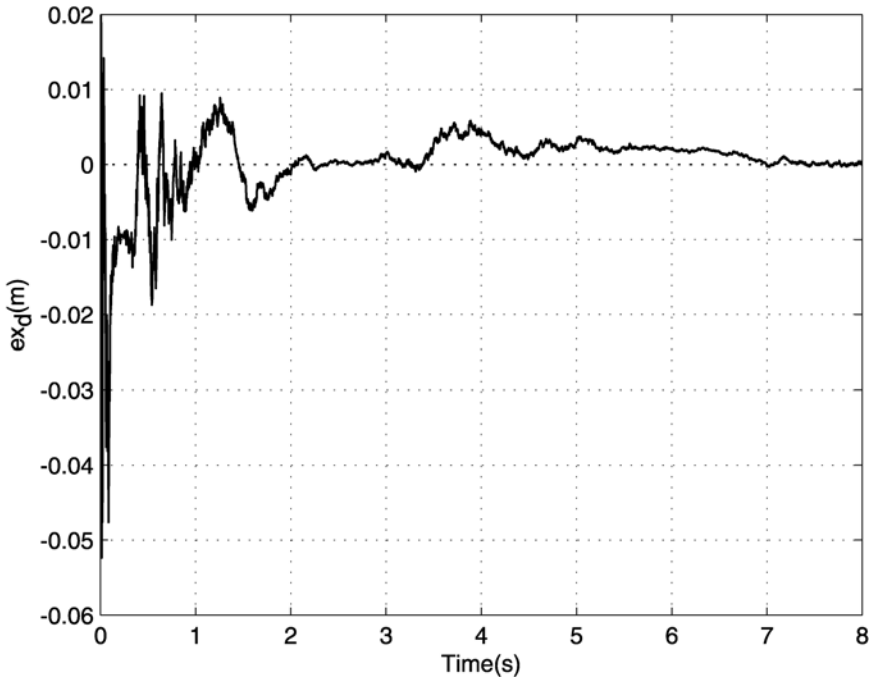

Figure 4.18. The mean position error using a continuous map to compare with Case 1.

segments for this localization technique. But the transition between two neighboring segments might decrease the efficiency of the localization. Hence there must be a compromise between the long polynomial map and the multisegment map for long trails. This will be the future work of this research.

Future work will also focus on experimental validation. An artificial mock-up will be built to simulate the uneven terrain. Experiments will be conducted on a two-axle CFMMR platform. A tilt sensor will be mounted on the rear axle of the robot to provide the estimated terrain inclination data for localization.

Another topic in the future work will be the application of terrain feature based localization to general robot motion where the robot tilts in two directions, such as pitch and roll. As the robot moves on a surface, the inclination vector needs to be measured

and combined with the inclination vector map to localize the robot position. The two-dimensional inclinations will increase the precision of the localization. However, the inclination map extraction will become more complicated considering the geometry of the robot. Therefore, the balance between the map extraction and the resulting precision must be considered.

4.5 Conclusions

This research proposes an EKF terrain feature based localization technique for a two-axle mobile robot operating in rough terrain. Simulation results validate the proposed technique and illustrate that the proposed technique has capability to reject system bias to achieve terrain feature localization. This technique can be generally applied to mobile robots in other uneven terrain environments. Future work will focus on applying this technique to long trails, validate them experimentally and extending it to two-dimensional analysis.

CHAPTER 5

CONCLUSIONS

In this dissertation, a nonlinear robust dynamic motion controller based on back-stepping technology is presented to deal with highly nonlinear interaction forces on Compliant Framed Modular Mobile Robots. A distributed cooperative motion control and sensing architecture is then presented to accommodate a kinematic motion controller, a dynamic motion controller and a sensor fusion system to achieve accurate robot motion. The dynamic motion controller presented above is used to implement the dynamic motion control subsystem in the proposed architecture. Experimental results prove the robustness and efficiency of path following and posture regulation performance. The final chapter of the dissertation proposes a terrain feature localization technique to future improve the position estimates of mobile robot such as the CFMMR operating on uneven terrain based upon the terrain characteristics. Simulation results verify the terrain feature localization technique and demonstrate its capability to achieve localization on uneven terrain. In this dissertation, the strategies, such as robust motion control, control and sensing architecture and terrain feature localization, are generally applicable to other mobile robotic systems while the target platforms are CFMMRs. The dissertation provides fundamental advancements on three major research aspects of robot motion control.

REFERENCES

[1] M. A. Minor, B. Albiston, and C. Schwensen, "Simplified motion control of a two axle compliant framed wheeled mobile robot," *IEEE Trans. on Robot.*, vol. 22, pp. 491-506, 2006

[2] X. Zhu, M. A. Minor, and S. Park, "Distributed robust control of compliant framed wheeled modular mobile robots," *ASME J. of Dyn. Syst., Meas., and Contr.*, vol. 128, pp. 489-498, 2006

[3] H. Kimura and S. Hirose, "Development of Genbu: Active wheel passive joint articulated mobile robot," in 2002 IEEE/RSJ Int'l Conf. on Intel. Rob. and Sys.(IROS 02), Sep 30-Oct 4, Lausanne, Switzerland, pp. 823-828 2002.

[4] H. Kimura, S. Hirose, and K. Shimizu, "Stuck evasion control for active-wheel passive-joint snake-like mobile robot 'Genbu'," in Proceedings- 2004 IEEE International Conference on Robotics and Automation, Apr 26-May 1 2004, New Orleans, LA, United States, pp. 5087-5092 2004.

[5] B. W. Albiston and M. A. Minor, "Curvature based point stabilization for compliant framed wheeled modular mobile robots," in *IEEE ICRA*, Sep 14-19 2003, Taipei, Taiwan, pp. 83-89 2003.

[6] A. Tayebi, M. Tadjine, and A. Rachid, "Invariant manifold approach for the stabilization of nonholonomic systems in chained form: Application to a car-like mobile robot," in *Proc. of the 1997 36th IEEE Conf. on Decision and Control*. Part 4 (of 5), Dec 10-12 1997, San Diego, CA, USA, pp. 4038-4043 1997.

[7] R. Fierro and F. L. Lewis, "Control of a nonholonomic mobile robot: backstepping kinematics into dynamics," *J. of Robot. Syst.*, vol. 14, pp. 149-163, 1997

[8] J.-M. Yang and J.-H. Kim, "Sliding mode motion control of nonholonomic mobile robots," *IEEE Control Syst. Mag.*, vol. 19, pp. 15-23, 1999

[9] M. Kumar and D. P. Garg, "Sensor-based estimation and control of forces and moments in multiple cooperative robots," *Transactions of the ASME. Journal of Dynamic Systems, Measurement and Control*, vol. 126, pp. 276-83, 2004

[10] Y. Hirata, Y. Kume, T. Sawada, Z.-D. Wang, and K. Kosuge, "Handling of an object by multiple mobile manipulators in coordination based on caster-like dynamics," in 2004 IEEE ICRA, Apr 26-May 1 2004, New Orleans, LA, United States, pp. 807-812 2004.

[11] C. P. Tang, R. Bhatt, and V. Krovi, "Decentralized kinematic control of payload transport by a system of mobile manipulators," in 2004 IEEE ICRA, Apr 26-May 1 2004, New Orleans, LA, United States, pp. 2462-2467 2004.

[12] A. Rodriguez-Angeles and H. Nijmeijer, "Mutual synchronization of robots via estimated state feedback: a cooperative approach," *IEEE Transactions on Control Systems Technology*, vol. 12, pp. 542-54, 2004

[13] A. G. O. Mutambara and H. E. Durrant-Whyte, "Estimation and control for a modular wheeled mobile robot," *IEEE Transactions on Control Systems Technology*, vol. 8, pp. 35-46, 2000

[14] H. G. Tanner, S. G. Loizou, and K. J. Kyriakopoulos, "Nonholonomic navigation and control of cooperating mobile manipulators," *IEEE Transactions on Robotics and Automation*, vol. 19, pp. 53-64, 2003

[15] K. Kosuge and M. Sato, "Transportation of a single object by multiple decentralized-controlled nonholonomic mobile robots," in 1999 IEEE/RSJ International Conference on Intelligent Robots and Systems (IROS'99): Human and Environment Friendly Robots whith High Intelligence and Emotional Quotients', Oct 17-Oct 21 1999, Kyongju, South Korea, pp. 1681-1686 1999.

[16] T. D. Murphey and J. W. Burdick, "The Power Dissipation Method and Kinematic Reducibility of Multiple-Model Robotic Systems," *IEEE Trans. on Robot.*, vol. 22, pp. 694-710, 2006

[17] X. Zhu, Y. Kim, and M. A. Minor, "Cooperative distributed robust control of modular mobile robots with bounded curvature and velocity," in 2005 IEEE/ASME International Conference on Advanced Intelligent Mechatronics, Monterey, California 2005.

[18] M. A. Minor and R. Merrell, "Instrumentation and Algorithms for Posture Estimation in Compliant Framed Modular Mobile Robotic Systems," *Submitted to the Int'l Journal of Robotics Research*, pp. 14, 2006,www.mech.utah.edu/~minor/publications/ijrr06.pdf

[19] Y. Kim and M. A. Minor, "Decentralized Kinematic Motion Control for Multiple Axle Compliant Framed Modular Wheeled Mobile Robots," in 2006 IEEE/RSJ International Conference on Intelligent Robots and Systems (IROS), Beijing, China 2006.

[20] X. Zhu, R. Merrell, and M. A. Minor, "Motion control and sensing strategy for a two-axle compliant framed wheeled modular mobile robot," in IEEE International Conference on Robotics and Automation, Orlando, Florida 2006.

[21] S. Park and M. A. Minor, "Modeling and dynamic control of compliant framed wheeled modular mobile robots," in *IEEE ICRA*, Apr 26-May 1 2004, New Orleans, LA, United States, pp. 3937-3943 2004.

[22] C. R. Weisbin, G. Rodriguez, P. S. Schenker, H. Das, S. A. Hayati, E. T. Baumgartner, M. Maimone, I. A. Nesnas, and R. A. Volpe, "Autonomous rover technology for Mars sample return," in iSAIRAS'99. Fifth International Symposium on Artificial Intelligence, Robotics and Automation in Space, 1-3 June 1999, Noordwijk, Netherlands, pp. 1-10 BN - 92 9092 760 7 1999.

[23] J. M. Roberts, P. I. Corke, J. Cunningham, and H. Durrant-Whyte, "Automation of underground LHD and truck haulage: Proceedings of the 1998 Annual Conference on Mining Cycle, AusIMM, Apr 19-23 1998," *Australasian Institute of Mining and Metallurgy Publication Series*. Mount Isa, Aust, 1998, pp. 241-245.

[24] D. S. Nasrallah, J. Angeles, and H. Michalska, "Modeling of an anti-tilting outdoor mobile robot," in DETC2005: ASME International Design Engineering Technical Conferences and Computers and Information in Engineering Conference, Sep 24-28 2005, Long Beach, CA, United States, pp. 2275-2284 BN - 0791847438 2005.

[25] K. Iagnemma and S. Dubowsky, *Mobile robots in rough terrain: estimation, motion planning, and control with applicaiton to planetary rovers*: Springer, 2004.

[26] A. Talukder, R. Manduchi, R. Castano, K. Owens, L. Matthies, A. Castano, and R. Hogg, "Autonomous terrain characterisation and modelling for dynamic control of unmanned vehicles," in 2002 IEEE/RSJ International Conference on Intelligent Robots and Systems, Sep 30-Oct 4 2002, Lausanne, Switzerland, pp. 708-713 2002.

[27] C. A. Brooks and K. Iagnemma, "Vibration-based terrain classification for planetary exploration rovers," *IEEE Transactions on Robotics*, vol. 21, pp. 1185-91, 2005

[28] C. Brenneke, O. Wulf, and B. Wagner, "Using 3D Laser Range Data for SLAM in Outdoor Environments," in 2003 IEEE/RSJ International Conference on Intelligent Robots and Systems, Oct 27-31 2003, Las Vegas, NV, United States, pp. 188-193 2003.

[29] K. Nagatani, H. Ishida, S. Yamanaka, and Y. Tanaka, "Three-dimensional localization and mapping for mobile robot in disaster environments," in 2003 IEEE/RSJ International Conference on Intelligent Robots and Systems, 27-31 Oct. 2003, Las Vegas, NV, USA, pp. 3112-17 BN - 0 7803 7860 1 2003.

[30] S. Thrun, W. Burgard, and D. Fox, *Probabilistic Robotics*: The MIT Press, 2005.

[31] J. Borenstein, H. R. Everett, and L. Feng, "Where am I? Sensors and Methods for Mobile Robot Positioning," University of Michigan, Ann Arbor, MI 1996.

[32] H. Surmann, A. Nuchter, and J. Hertzberg, "An autonomous mobile robot with a 3D laser range finder for 3D exploration and digitalization of indoor environments," *Robotics and Autonomous Systems*, vol. 45, pp. 181-98, 2003

[33] Y. Zhuang, W. Wang, K. Wang, and X.-D. Xu, "Mobile robot indoor simultaneous localization and mapping using laser range finder and monocular vision," *Zidonghua Xuebao/Acta Automatica Sinica*, vol. 31, pp. 925-933, 2005

[34] D. Burschka and G. D. Hager, "V-GPS(SLAM): vision-based inertial system for mobile robots," in 2004 IEEE International Conference on Robotics and Automation, 26 April-1 May 2004, New Orleans, LA, USA, pp. 409-15 BN - 0 7803 8232 3 2004.

[35] A. Cumani, S. Denasi, A. Guiducci, and G. Quaglia, "Integrating monocular vision and odometry for SLAM," *WSEAS Transactions on Computers*, vol. 3, pp. 625-30, 2003

[36] S. Panzieri, F. Pascucci, I. Santinelli, and G. Ulivi, "Merging topological data into Kalman based SLAM," in Proceedings of the World Automation Congress, 28 June-1 July 2004, Seville, Spain, pp. 57-62 2004.

[37] A. Diosi and L. Kleeman, "Advanced sonar and laser range finder fusion for simultaneous localization and mapping," in 2004 IEEE/RSJ International Conference on Intelligent Robots and Systems (IROS), 28 Sept.-2 Oct. 2004, Sendai, Japan, pp. 1854-9 BN - 0 7803 8463 6 2004.

[38] P. Bonnifait, P. Bouron, P. Crubille, and D. Meizel, "Data fusion of four ABS sensors and GPS for an enhanced localization of car-like vehicles," in

Proceedings 2001 ICRA. IEEE International Conference on Robotics and Automation, 21-26 May 2001, Seoul, South Korea, pp. 1597-602 BN - 0 7803 6576 3 2001.

[39] D. Bouvet and G. Garcia, "Civil-engineering articulated vehicle localization: solutions to deal with GPS masking phases," in Proceedings 2000 ICRA. IEEE International Conference on Robotics and Automation, 24-28 April 2000, San Francisco, CA, USA, pp. 3499-504 BN - 0 7803 5886 4 2000.

[40] E. Theunissen, G. J. M. Koeners, R. M. Rademaker, R. D. Jinkins, and T. J. Etherington, "Terrain following and terrain avoidance with synthetic vision," in The 24th Digital Avionics Systems Conference, 30 Oct.-3 Nov. 2005, Washington, DC, USA, pp. 4-2 BN - 0 7803 9307 4 2005.

[41] R. E. Zelenka, R. F. Clark, A. Zirkler, R. Saari, and R. G. Branigan, "Development and flight test of terrain-referenced guidance with ladar forward sensor," *Journal of Guidance, Control, and Dynamics*, vol. 19, pp. 823-828, 1996

[42] F. M. Cancilliere, "Advanced UUV technology," in Proceedings of OCEANS'94, 13-16 Sept. 1994, Brest, France, pp. 147-51 BN - 0 7803 2056 5 1994.